arXiv:2001.10954v1 [q-bio.QM] 29 Jan 2020

Reducing complexity and unidentifiability when modelling human atrial cells.

C. Houston[1,2], B. Marchand[2], L. Engelbert[2], C. D. Cantwell[1,2]

[1]ElectroCardioMaths Programme, Centre for Cardiac Engineering, Imperial College, London.
[2]Department of Aeronautics, Imperial College, London.

Abstract

Mathematical models of a cellular action potential in cardiac modelling have become increasingly complex, particularly in gating kinetics which control the opening and closing of individual ion channel currents. As cardiac models advance towards use in personalised medicine to inform clinical decision-making, it is critical to understand the uncertainty hidden in parameter estimates from their calibration to experimental data. This study applies approximate Bayesian computation to re-calibrate the gating kinetics of four ion channels in two existing human atrial cell models to their original datasets, providing a measure of uncertainty and indication of potential issues with selecting a single unique value given the available experimental data. Two approaches are investigated to reduce the uncertainty present: re-calibrating the models to a more complete dataset and using a less complex formulation with fewer parameters to constrain. The re-calibrated models are inserted back into the full cell model to study the overall effect on the action potential. The use of more complete datasets does not eliminate uncertainty present in parameter estimates. The less complex model, particularly for the fast sodium current, gave a better fit to experimental data alongside lower parameter uncertainty and improved computational speed.

Keywords: cardiac modelling, approximate Bayesian computation, uncertainty, unidentifiability, action potential

1 Introduction

A central component in simulations of cardiac electrophysiology is a model of an action potential (AP) for a representative cardiomyocyte. These models describe how the transmembrane potential, and other physiological properties of a cardiac cell, vary through time due to changing environmental conditions or applied stimuli. Since the development of the initial, relatively simple, model of a neuron [1], AP models have grown in scope and complexity as new experimental data have become available [2].

Uncertainty is an unavoidable aspect of scientific experiments, particularly in the biological sciences. Further understanding in this area has been designated a priority as cardiac models advance towards safety-critical applications [3]. Uncertainty is introduced by variability inherent in the biological system (e.g. differences in AP waveforms between different myocytes), the stochastic nature of biological processes (e.g. opening and closing of ion channels) and imperfect recording systems (e.g. noise in voltage patch clamp experiments) [3]. It is common for AP models to use equations with a large number of parameters to describe the flow of ions across the cell membrane. This is a particular challenge for model calibration in which parameters are tuned to reflect experimental observations, usually by comparing model output to experimental measurements using a regression method (e.g. least-squares). The consequence of the uncertainty and high number of parameters is that multiple different parameter combinations may produce the same residual to experimental data; a unique optimum parameter set may not exist.

Traditional fitting techniques, such as simple least squares regression, implicitly assume that a single point estimate exists for each parameter in a model [4]. In cardiac modelling, this is unlikely to be the case for reasons outlined above. Bayesian methods can quantify uncertainties in parameter estimates by determining a posterior distribution over parameter values given the available data [5]. These distributions can highlight unidentifiable parameters, those without a single unique optimum, and make it possible to capture the effect of experimental and biological variability on model parameters. Unidentifiability may be either structural, caused by an overly complex model where parameters can be varied

simulataneously without a change in model output, or practical, where insufficient data is available to determine a parameter's value. In cardiac cell modelling, it can be difficult to obtain an exact likelihood function necessary for exact Bayesian inference when summary statistics are used, as is commonplace in studies of cardiac ion channels. This is further complicated by the high-dimensional parameter space, nonlinear nature and indirect observation properties of AP models [6]. Instead, one can employ approximate Bayesian methods, such as approximate Bayesian computation (ABC), which provide a reasonable estimate to the posterior distributions of parameter values [7].

When developing a model of a new cell type, the most common approach is to 'inherit' gating kinetic formulations from existing models and tune channel conductances to data from multiple sources [8]. However, equations describing gating kinetics of ion channels can be extremely complex and often contribute the majority of the parameters in AP models. In contrast to channel conductances, which can be adjusted to measurements of APs, gating kinetics are typically calibrated to data from voltage patch clamp experiments. In these experiments, channels are isolated, by pharmacological means or the use of specific voltage step protocols, to take measurements of individual current traces. Previous studies [9, 10, 11] have been valuable in developing approaches to investigate parameter identifiability in both generalised Hodgkin-Huxley models and more detailed widely-used channel models. We build on this field of work to include consideration of the available experimental data across a range of simple and complex channel models of a human atrial cell.

In this study, we apply an approximate Bayesian method to investigate the uncertainty and parameter unidentifiability present in channel gating kinetics in a human atrial cardiomyocyte. Computational experiments are carried out on two human atrial cell models, the Nygren [12] and Courtemanche [13] models, henceforth referred to as the N and C models respectively. These were the first two biophysical models developed to simulate the AP from a human atrial myocyte and have proved influential in the development of subsequent models and whole-heart tissue-scale modelling. The N and C models are detailed cell models, each including descriptions of twelve ion currents which contribute to the AP in human atrial myocytes. We thus only focus our study on the four major ion currents which are prominent determinants of their AP morphology [14, 15]: the fast sodium channel (I_{Na}), L-type calcium channel (I_{CaL}), transient outward potassium channel (I_{to}) and ultra-rapid delayed rectifier potassium channel (I_{Kur}).

We first re-calibrate parameters in each channel model to experimental datasets used in the original publications to investigate the existing level of uncertainty and parameter unidentifiability. To explore whether these issues can be alleviated from inclusion of more data, which would suggest practical unidentifiability, a 'unified' dataset is formed and the models re-calibrated to these data. To investigate whether these models suffer from structural unidentifiability, a model of reduced complexity [16] is calibrated to the same unified dataset, and parameter posterior distributions and the overall goodness-of-fit of the model compared to the re-calibrated N and C models. These re-calibrated channel models are then inserted into the full N and C cell models to study the effect of the re-calibration on AP morphology. We conclude by discussing the relative advantages and drawbacks of these approaches and limitations of the study.

2 Methods

2.1 Action potential models

The AP models studied in this work follow the commonly-used Hodgkin-Huxley gating form [1]. The changing transmembrane voltage is calculated from the solution of several coupled ordinary differential equations describing individual ion currents. Each current is of the common form

$$I_i = g_i \prod_j \gamma_j^{k_j} f(V_m), \qquad \frac{d\gamma_j(t)}{dt} = \alpha_{\gamma_j}(V_m;\boldsymbol{\lambda})\,[1-\gamma_j] - \beta_{\gamma_j}(V_m;\boldsymbol{\lambda})\gamma_j, \tag{1}$$

where g_i is the maximum channel conductance which scales the current amplitude (S/F); γ_j are gates of the channel determined by voltage-dependent forward and backward transition rates between open and closed states, α and β, characterised by gating parameters $\boldsymbol{\lambda}$; k_j is an exponent term that may be applied to represent multiple identical gates in parallel; and f is some voltage-dependent forcing function (most commonly the difference between V_m and the ion Nernst potential). The gating equation may equivalently be transformed into a form explicitly specifying steady-state values, γ_∞ and time constants, τ_γ

$$\frac{d\gamma(t)}{dt} = \frac{\gamma_\infty(V_m) - \gamma}{\tau_\gamma(V_m)}, \qquad \tau_\gamma(V_m) = \left[\alpha_\gamma(V_m;\boldsymbol{\lambda}) + \beta_\gamma(V_m;\boldsymbol{\lambda})\right]^{-1},$$
$$\gamma_\infty(V_m) = \alpha_\gamma(V_m;\boldsymbol{\lambda})\tau_\gamma \qquad \text{if activating gate,}$$
$$\gamma_\infty(V_m) = \beta\gamma(V_m;\boldsymbol{\lambda})\tau_\gamma \qquad \text{if inactivating gate,} \tag{2}$$

(where we omit the indexing subscript for clarity). There are no standard formulations for the voltage-dependent transition rates $\alpha_\gamma(V_m;\boldsymbol{\lambda})$ and $\beta_\gamma(V_m;\boldsymbol{\lambda})$, and each model implements a different set of equations [12, 13]. For I_{Na}, and for the C model also I_{CaL}, the structure of these equations was inherited directly from the parent model (of a rabbit atrial cell [17] and guinea pig ventricular cell [18] for the N and C model respectively), while I_{to}, I_{Kur} and, for the N model, I_{CaL} were introduced as new formulations in each model. The equations are included in Section S4. In this work, we are interested in the ability of the gating kinetics to reflect the experimental data, and the identifiability of parameters $\boldsymbol{\lambda}$ with respect to this data.

The standardised formulation, henceforth referred to as the S model, is used as a relatively simple baseline to compare to the more complex formulations in the N and C models. In this formulation, the transition rates between open and closed states have a structure based on free energy arguments [19, 20], which has been shown as sufficient to capture the kinetics of a rapid delayed rectifier potassium current [16]. The transition rates are given by

$$\alpha(V_m) = \lambda_1 \exp(\lambda_2 V_m), \qquad \beta(V_m) = \lambda_3 \exp(-\lambda_4 V_m), \tag{3}$$

where the parameters requiring calibration are $\lambda_1, ..., \lambda_4$ for each gate in the channel model. For I_{Na} and I_{CaL} which have two components of inactivation, we add another inactivation gate in parallel for the S model, which is related directly to the existing inactivation gate by a scale parameter on its magnitude, e.g. $\tau_{\gamma 2} = a\tau_{\gamma 1}$ where a is the scale parameter. Only the activation gate of the S model for I_{Na} has a power of 3 applied to remain consistent with both N and C models.

2.2 Datasets and calibration

Parameters underlying gating kinetics are calibrated to experimental data from voltage patch clamp experiments conducted on isolated cardiomyocytes. Though more complex protocols may be better able to explore the entire range of kinetics exhibited by different ion channels [16], the majority of available data were generated through the use of 'traditional' voltage stepping protocols. In these experiments, the transmembrane potential is held fixed and subsequently clamped to a series of voltage steps while the current across the membrane is recorded. Specific features of the recorded current can then be calculated and summarised across different cells or experiments.

Data from voltage patch clamp experiments in human atrial myocytes for I_{Na} [21, 22], I_{CaL} [23, 24, 25], I_{to} [26, 27, 28] and I_{Kur} [27, 28] were digitised (including any error measurement). A virtual voltage clamp protocol was created to replicate *in-silico* each of the *in-vitro* experiments. A full description of data sources and voltage clamp protocols are included in Section S1. The N model did not include calibration data for any time constants in I_{Na}, for activation time constants in I_{to} and for deactivation of I_{Kur}. The C model did not calibrate to voltage-dependent recovery data in I_{CaL} and I_{Kur}. Neither model included an activation time constant measurement available for I_{CaL}.

We use approximate Bayesian computation (ABC) to calibrate each channel model to the experimental data. ABC replaces an exact likelihood function by sampling parameter values from a chosen prior distribution and simulating the model under the specific voltage clamp protocol. These simulated data are processed into summary statistics which can be compared to experimental data using a distance function. The prior distribution for each parameter is set to a uniform distribution. For the N and C models, the width of the prior is set based on the published value of the parameter and its position in the model structure. The width was increased if it was noted that during calibration the distribution was being restricted by the upper or lower prior limit. For the S model, the prior ranges were set as previously [16, 29].

The summary statistics are calculated from the output of a function that makes specific measurements, for example peak current or decay rate from fitting an exponential equation, of the current trace in response to the voltage clamp protocol replicated from the experimental publication. The summary statistic functions are assumed invariant to the magnitude of current, and thus channel conductance is

not included as a calibration parameter. A low distance value generated by the distance function indicates that a particular sample from the parameter space is more likely to be from the 'true' distribution. This behaviour is captured algorithmically by using a threshold value which is used to decide whether to accept or reject a specific sample. For a more detailed overview of ABC, see e.g. [7].

An advantage of ABC is prior knowledge of the experimental data can be embedded in the distance function during calibration. Data from voltage-clamp experiments includes error bars to account for the different results from experimental repeats due to observational noise and other sources of experimental uncertainty [3]. We are more certain of the value of data points with low variance (small error bars) from the experimental data sets. To account for this, we use a weighted least squares distance function with weights proportional to the inverse of the standard deviation at experimental data points. A regularisation parameter is included to avoid divide-by-zero errors and set to 0.05. To avoid bias to individual experiments with more data points, this weighting is also proportional to the number of data points in an experiment. Further details are included in Section S2.

2.3 Implementation

Voltage clamp experiments were simulated using the myokit Python library [30]. The ABC sampling process uses the pyABC Python library [31] to implement the Toni ABC sampler based on sequential Monte Carlo [32]. In this sampler, the ABC process above is repeated through a number of iterations with reducing threshold value. Further details are included in Section S2. We created the *ionchannelABC* Python library for applying ABC in this context which integrates pyABC and myokit for voltage patch clamp ABC calibration (see Data Accessibility).

When comparing the relative computational speed to solve different channel models, we apply a voltage pulse train protocol of 100 pulses (using channel-dependent voltage steps indicated in the text). We record the time taken for a simulation from each of the 100 samples from the posterior parameter distributions to account for variability.

To simulate the effect on the AP of re-calibrated channels, each new parameterisation was inserted into either the entire N or C model. Channels were tested one at a time, and parameters in other channels left at their published values. 100 samples were taken from the unified posterior distribution and a pulse train protocol applied to generate AP samples from the full model. The pulse train consisted of 1ms current stimuli at a rate of 1 Hz and with amplitude 40 pA/pF. The AP elicited during the 100th pulse was recorded for analysis.

S channel models were then used in place of the published formulas to study the effect of a reduction in complexity on the overall AP. In all cases, the conductance of the channel was set by matching the peak current magnitude from each sample to the peak from the published channel model (peak current was assumed to occur at 60mV for I_{to} and I_{Kur} models). This experiment could not be conducted for I_{Na} as both the N and C modellers positively shifted the steady-state curves according to macro measurements of the AP (such as velocity of the upstroke), and in the previous section this channel was calibrated to the original experimental data. As in this study voltage clamp protocols were replicated exactly as described in the experimental publications, it is not clear how these would be adapted to fit the artificially-shifted data, or how to manually shift the steady-state curves.

All figures display experimental measurements as mean ± standard deviation reported in the experimental publication. The calibrated model is displayed by taking 100 samples from the posterior distribution of parameters and plotting the output from simulations as median ± 89% high density posterior intervals (HDPI) [33].

3 Results

3.1 Existing gating parameter uncertainties

We first sought to study uncertainty and unidentifiability present in gating parameters of the existing models using the datasets originally cited for calibration [12, 13]. Only I_{Na} and I_{to} channels of the C model are calibrated to the full range of data available (Table S1). It would be expected that a higher level of uncertainty is present in kinetics of the channel within voltage ranges that have not been explicitly tested. A high level of uncertainty in the parameter value is indicative of potential structural or practical unidentifiability.

For example, the I_{Na} channel in the N model was only directly compared to steady-state experimental data [21]. Figures 1A and 1B show representative posterior distributions and kernel density estimates

(KDEs) of those distributions following ABC calibration for this channel. Parameters underlying steady-state components of the channel (Figure 1A) exhibited narrow posterior distributions indicating they were well-constrained by the data. In contrast, parameters underlying time constants had relatively wide posterior distributions implying they are poorly constrained (Figure 1B) and suggesting there is a higher level of uncertainty surrounding their value in the model (see Section S4.1 for equations). The effect of the poorly constrained time constant parameters can be seen in Figure 1C which shows the response of the calibrated N model of I_{Na} to the voltage clamp protocols. The decay rate of the current is highly variable, consistent with the observation of poorly constrained time constant parameters. Figure 1D shows how this uncertainty is 'hidden' by the steady-state summary statistics function used to process the traces in experiments. Note that the non-physiological error bars of the experimental data are a result of plotting as mean ± standard deviation.

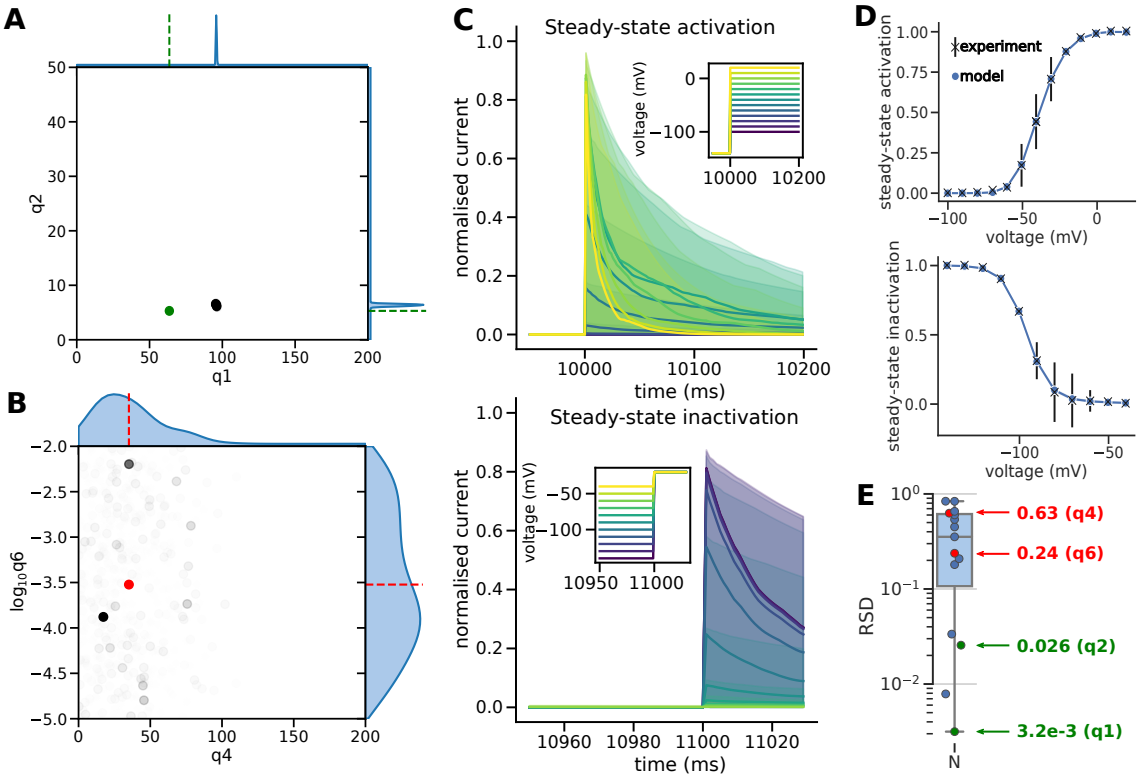


Figure 1: **A,B** Examples of parameter posterior distributions from the N model of I_{Na} after calibration to the original dataset which only included steady-state data. Scatter plots show the population of posterior ABC particulars with weights indicated by opacity. 1D KDEs of each parameter posterior distribution are displayed along the corresponding axes. The original parameter values from the model are indicated as dots and dashed lines. **C** Normalised current traces of posterior model response to inset voltage protocol displayed as median line with shading indicating 89% HDPI from 100 samples from parameter posterior distributions. The high variability in decay rate is the result of no time constant data included in the dataset used for calibration. **D** Summary statistics generated from results in C. **E** RSD values of all parameter posteriors with representative parameters from A and B highlighted.

Relative standard deviation (RSD; defined as $\sigma/|\mu|$) is a scale invariant measure of the width of the parameter posterior distributions and used to provide a comparison of the parameter uncertainty between models. Higher RSD values can indicate that a particular parameter is unidentifiable with respect to the model structure or available data. Figure 1E shows the RSD values for all parameter posterior distributions in the calibrated N model, and highlights the values for distributions shown in Figures 1A and 1B. The parameters with narrower posterior distributions have RSD values orders of magnitude lower than those with wide posteriors (note the log scale on the y-axis). In this case, the four parameters with an RSD less than 10^{-1} can be interpreted as governing the shift and steepness of the steady-state activation and inactivation curves in Figure 1D, and it is thus not surprising that these were more identifiable than parameters involved in rise and decay rates of the current.

3.2 Re-calibrating to a unified dataset

Having observed a range of poorly and well-constrained parameters when calibrating to the original datasets, we next sought to investigate the effect of re-calibrating each model to a different 'unified' dataset. This dataset is assembled from a union of the original experimental data sources.

Figure 2A shows the RSD of parameter posteriors for all channels studied in the N and C models when calibrated to the original and unified datasets. In all models, a wide range of RSD values is observed for the original datasets which confirms each model has a combination of parameters which are well-defined and parameters which are potentially unidentifiable with respect to the given data. In the N model, no significant differences in the parameter posterior RSDs were observed between original and unified dataset calibrations for I_{Na} and I_{to} using a Wilcoxon signed-rank test. In both I_{Na} and I_{CaL} the minimum RSD increased after calibrating to the unified dataset. In I_{CaL} and I_{to}, we also noted an increase in the maximum RSD. No significant differences were observed for the C model. Note that a Wilcoxon signed-rank test was not carried out for I_{CaL} (for the N model) or I_{Kur} as this statistical test requires discarding differences between pairs of zero and the resulting sample size was too small for a normal approximation. This is a result of only re-calibrating parameters of one gate to unified data in these models as the unified data for the other gate was the same as the original dataset (thus the RSD values of parameters in the other gate remains constant between the original and unified dataset).

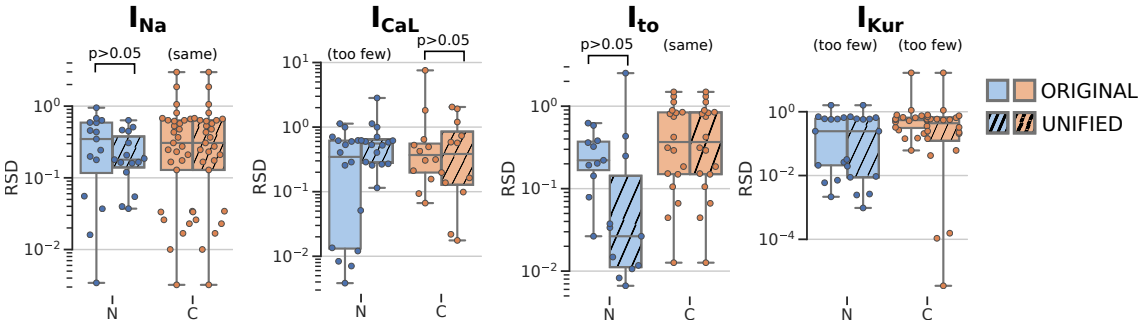


Figure 2: RSDs of each parameter in each channel model for original and unified experimental datasets in both N and C models. Significance tested with Wilcoxon signed rank test. Text 'too few' above a pair of boxplots indicates that the sample size was too small to conduct the statistical test after eliminating differences of zero.

Regions of high uncertainty in gating functions generally corresponded to behaviour or voltage ranges not tested by the experimental voltage-clamp protocols. Adding the additional data in the unified dataset generally reduced the variability in these regions, though often at the expense of other aspects of the model. For example, the N model of I_{Na}, showed high uncertainty in the posterior estimates for time constant functions with the original dataset, which was reduced on calibration to the unified dataset. However, this reduction came at the expense of greated variability in the steady-state behaviour of the channel. A similar effect was noticed in the inactivation processes of the C model of I_{CaL}. For the N model of I_{to} and the inactivation of the C model of I_{Kur}, calibrating to the unified dataset resulted in noticeable changes to the shift and steepness of the steady-state functions. Full graphs of the posterior gating functions are included in Section S3.1.

3.3 Comparing to a standardised model

No statistically significant reduction in RSD values for parameter posterior distributions was observed when re-calibrating the N and C models to more complete datasets. This implies that the additional data covering a wide range of kinetics for each channel was not sufficient to reduce unidentifiability observed in parameters. We hypothesised that this could be due to problems with structural unidentifiability caused by the complex form of the equations in either model. To test this, we next studied whether a simpler model structure of the S model could be used to reflect the same experimental data with reduced parameter uncertainty for each channel.

Fast sodium channel. Figure 3A compares I_{Na} models calibrated to the unified experimental dataset. The goodness-of-fit of each model can be assessed by comparing the final converged residual obtained during ABC, shown in the rightmost graph of Figure 3D (a per-experiment version of this measure for all channels is given in Section S3.5). In most experiments, the S model qualitatively reflects

the experimental data to a comparable degree as the N and C models, improving notably over the N model in recovery experiments. The overall converged residual of the S model is 23.5% lower than the N model and 30.0% lower than the C model. It notably deviates from experimental data in the upper voltage range of the activation time constant where it falls too quickly towards zero. We observe that although the S model has in total 9 parameters compared to 15 in the N model and 29 in the C model (Figure 3D, left), the S model has more tightly constrained parameter posterior distributions exhibiting lower RSD (Figure 3D, centre). This reduction of RSD values was statistically significant when tested using a Mann-Whitney U-test against the N model ($p = 0.02$) and C model ($p = 0.04$).

Figure 3B compares the underlying gate functions of each I_{Na} model. The S model exhibits generally well-constrained behaviour other than in the region of a gap in experimental data (deactivation data in lower voltages of the activation gate time constant). Only the C model exhibits low uncertainty in this region. In this case, the uncertainty may not be beneficial as it could imply undue confidence in the C model's behaviour in model space without experimental data to compare. There is a distinct difference in the form of the N model inactivation gate time constants which have a sigmoid shape rather than the peaked curve exhibited by both C and S models. Comparing the current trace of each model at the end of a pulsetrain (Figure 3C), there is little difference between the fully calibrated traces of the C and S models, and the S model has a significantly reduced runtime for this protocol.

L-type calcium channel. I_{CaL} has calcium- as well as voltage-dependent components of inactivation. The N and C models differ in how they formulate this channel; the former including two voltage-dependent inactivation gates and the latter including a single voltage-dependent inactivation gate. Both include a single calcium-dependent inactivation gate that was held at a constant value to isolate the voltage-dependent features of the channel. Given the data typically shows a fast and slow component of inactivation [24], we include two voltage-dependent inactivation gates in the S model of I_{CaL}. Thus comparisons are more meaningful between the N and S models in this case, as the structure of the C model differs substantially and relies more directly on intracellular calcium concentration to modulate the rate of current decay.

Figure 4 summarises the results for I_{CaL}. None of the models appear able to calibrate to the slowest components of recovery from inactivation (Figure 4A). The gating functions in Figure 4B show high uncertainty in the steady-state function of the S model and differs from the N and C models at higher voltages of the inactivation steady-state curve. Each model has reduced uncertainty around the voltages of time constants which are explicitly tested (inactivation and recovery τ measurements) with, particularly in the N model, wide uncertainty outside of these ranges. Figure 4C shows there were no significant differences between RSD values between the models, highlighting that each model suffers from issues with parameter identifiability in some parts. The N and S models provided better fits to the data when assessed by the final converged residual though, as noted above, the C model relies more heavily on the calcium-dependent inactivation processes held constant in this experiment.

Potassium channels. Figure 5 summarises the results from the calibration for I_{to}. Although the N and S models both show parameter posteriors with significantly lower RSD values than the C model, this is balanced by the lower goodness-of-fit to the experimental data (Figure 5B, lower). In particular, the S model was unable to capture kinetics such as the plateau region of the upper voltage range for the inactivation time constant. In contrast, the C model has the most parameters and appears to suffer from unidentifiability in a subset of these parameters (suggested by their high RSD values), but it also produces the best fit to the experimental dataset.

The underlying gating functions also reveal clear differences between models in the midpoint and slope of steady-state activation, and peak activation time constant (Figure S9). The peak time constants of each model are approximately at the midpoint voltage of activation and thus also differ from each other.

I_{Kur} exhibits a very slow voltage-dependent component of inactivation and only partially inactivates in the available voltage clamp experimental data [28]. As a result of these factors, each channel model showed distinct differences when calibrated to experimental data using the experimental voltage protocols rather than comparing gating functions to experimental data directly. Each channel deviates from experiment data points at lower voltage ranges of steady-state activation, and the S model converged to a substantially different model output for the steady-state inactivation gate (Figure S10).

3.4 Effect on action potential

We next studied how the inclusion of uncertainty in the gating of these channels would impact the full AP of the cell models. Figure 6 shows how the AP changed for the channel models for the re-calibrated N

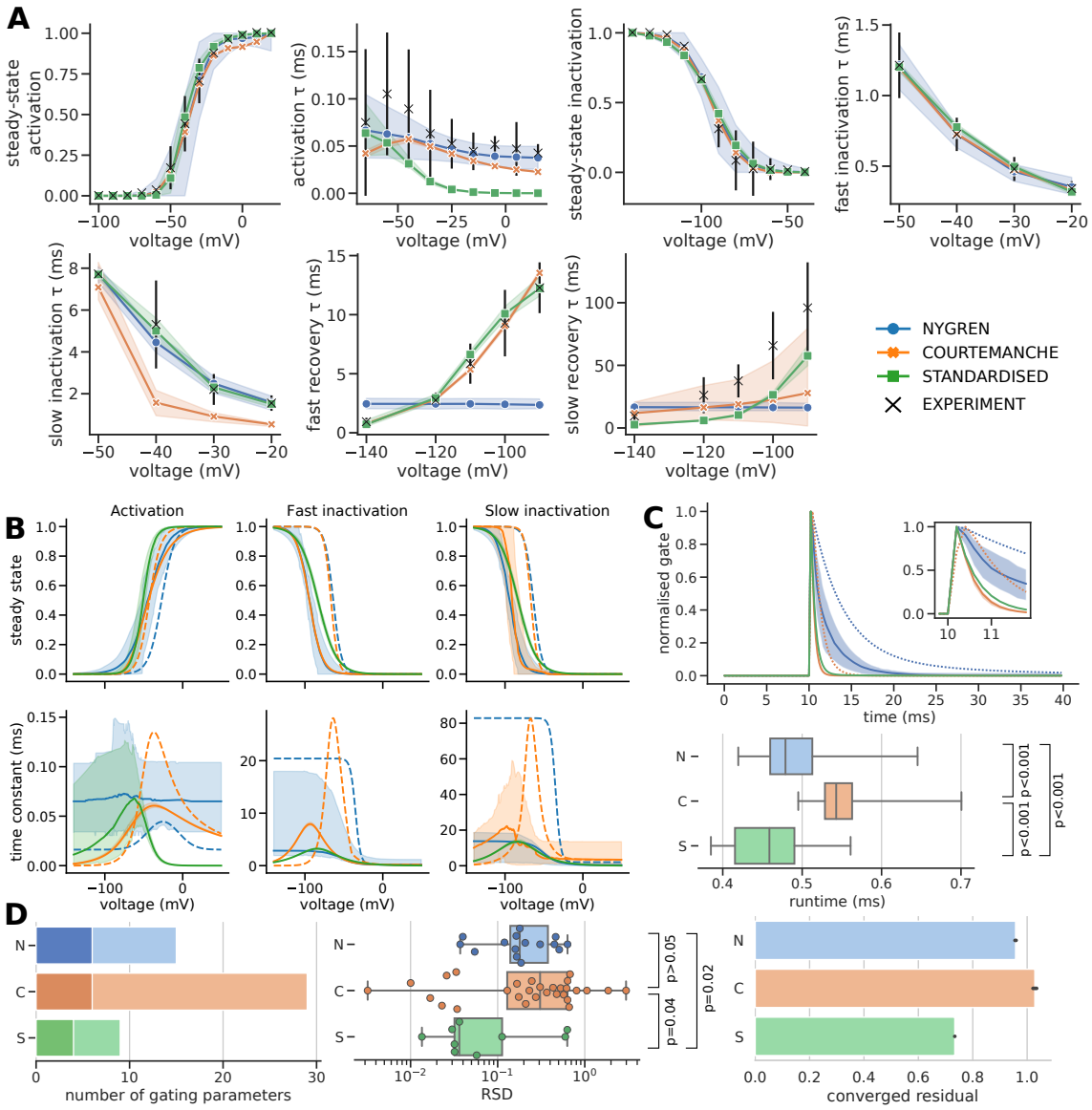


Figure 3: **A** Results of calibrating each I_{Na} model to the unified dataset. Model output is plotted as median line and 89% HDPI from 100 parameter posterior samples. Experimental data is plotted as black crosses and bars representing mean and SD. **B** Steady-state and time constant functions for each gate from samples in A. Dashed lines indicate the published N and C models. **C** Example traces from each model generated from the last step of a pulse train of 100 steps from -140 mV to -30 mV for 100 ms at a rate of 1 Hz using samples from A. Dashed lines indicate the published N and C models. Boxplot compares time taken to run the protocol for each model. **D** Number of gating parameters in each model (left). Dark and light shading correspond to activation/inactivation gating parameters respectively. RSD of parameter posteriors in each model (centre). Goodness of fit assessed by the converged residual of ABC (right). Significance tested using Mann-Whitney U-test.

channels, re-calibrated C channels, and inserting the re-calibrated S channel into either model (referred to as N+S and C+S). As noted in the Methods, this experiment could not be completed for I_{Na} models. More detailed results are in Section S3.6.

For I_{CaL} a portion of posterior samples in the N model resulted in an elevated resting potential, though the median was still close to the published value. This causes the wide 89% HDPI observed in the corresponding trace, while the median line is much closer to the dashed line of the original model. This also occurred to a lesser degree when the S model inserted into the C cell model. The re-calibrated

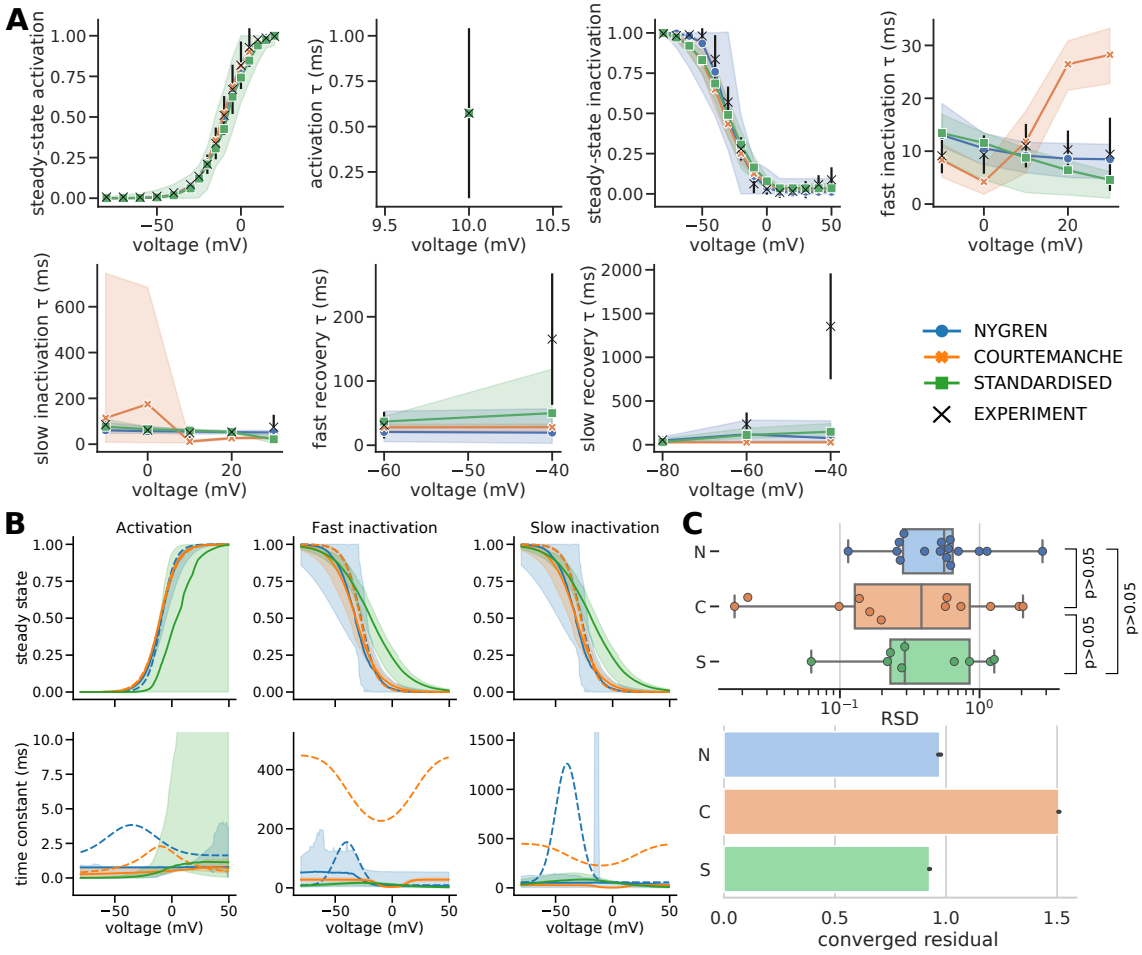


Figure 4: **A** Results of calibrating I_{CaL} models to the unified dataset. Plotted as described in Figure 3. **B** Steady-state and time constant functions for each gate from the samples in A. Dashed lines indicate published N and C models. **C** RSD of parameter posteriors (upper). Goodness of fit assessed by converged residuals from ABC (lower).

C model was more stable with the action potential duration (APD) being mainly reduced from the published value as a result of quicker and more complete inactivation of the channel during the AP (Figure 13B).

Traces generated by using the posterior parameterisations for I_{to} generally showed small differences from the published values for resting potential and AP amplitude, though larger changes in the APD. For the full N model (both with the original channel form and S form), an increased APD is observed while the opposite was observed for the C model. This makes the two AP models, which have quite different published AP morphology, more similar to one another. A small degree of variability is apparent from the posterior intervals around the traces and, in contrast to I_{CaL} all samples resulted in 'normal' APs.

Using the re-calibrated form of I_{Kur} resulted in more noticeable changes to the AP than I_{to}. For both the N and N+S experiments, this increases the resting potential and AP amplitude accompanied by an increase in APD to a similar level as the published C model. In both cases, the triangular morphology of the published N model was altered to have a more prolonged plateau phase. For the C model, the resting potential and amplitude of the AP from close to the published values, while a large degree of variability is observed in the APD. When using the C form of the channel, this variability encompassed the published value, which is apparent from the shading of the AP trace including the dashed trace of the published C model. When using the S form of the channel, the cell repolarises more quickly as a result of an increased I_{Kur} current density.

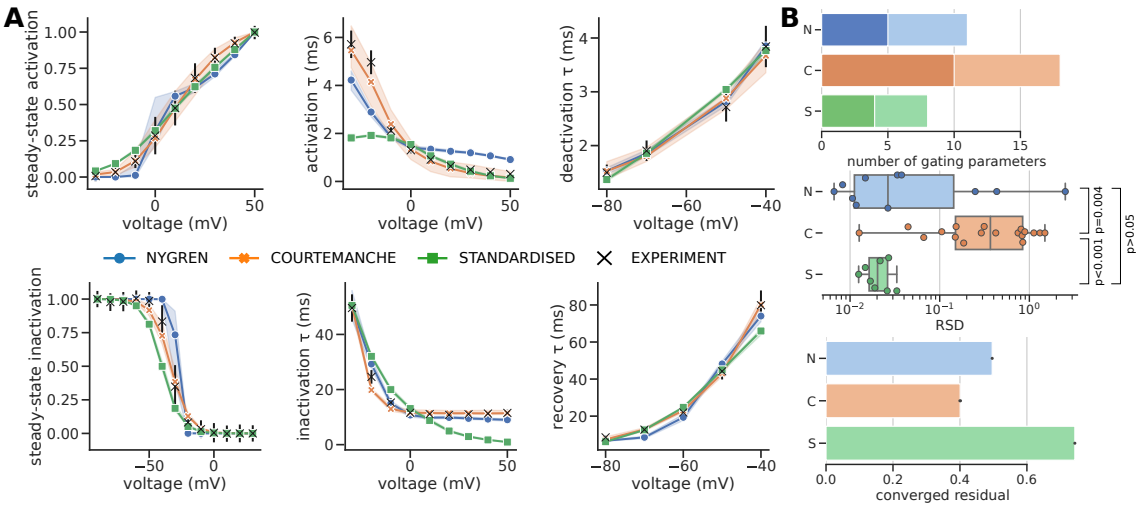


Figure 5: **A** Results of calibrating each I_{to} model to the unified dataset. Plotted as described in Figure 3. **B** Number of gating parameters (top). RSD of parameter posteriors (centre). Goodness of fit assessed by converged residuals from ABC (bottom).

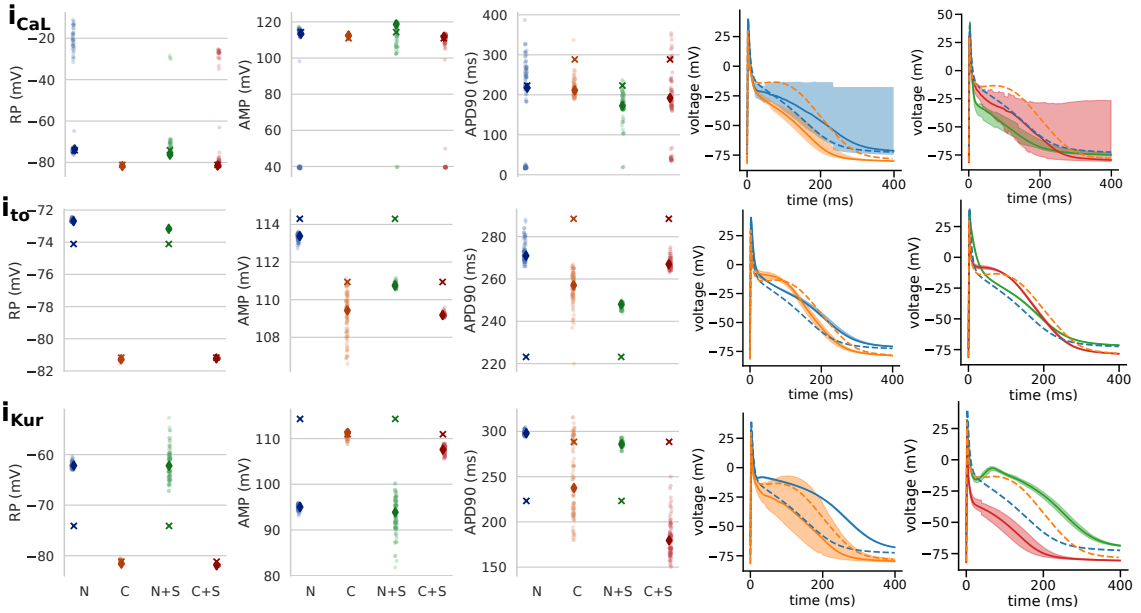


Figure 6: Strip plots showing measurements of resting potential (RP), action potential amplitude (AMP) and AP duration to 90% repolarisation from APs elicited from the full N and C models. Crosses indicate values from the models run at published settings. Each point is a measurement from an AP generated from a sample from the posterior parameter distribution of the channel indicated in bold. The diamond is the median of the samples. N: using N unified posterior distribution in the full N model, C: using C unified posterior distribution in the full C model, +S: indicates the standardised model replaced the corresponding channel in the full model and used the S posterior distribution. Line plots in the two rightmost columns display a summary of the AP traces in each case. Traces are displayed as median lines with shading representing 89% HDPI from 100 posterior samples. The published N and C models are plotted as dashed lines in all plots for comparison.

4 Discussion

Understanding the uncertainty and unidentifiability of parameters in AP models is critical to the development of trustworthy cardiac models for the era of personalised medicine [5, 3]. In this study, we

have applied an ABC method based on sequential Monte Carlo to characterise the existing uncertainty in gating kinetics of four major ion channel types in human atrial cell models. The wide posterior distributions for a subset of parameters in all models was indicative of potential unidentifiability, which may be structural or practical. We then sought to assess whether the poorly constrained parameters could be more clearly identified by re-calibrating to complete datasets or through using a standardised gating formulation with less complex structure and fewer parameters to constrain. We finally looked at the changes introduced by using the re-calibrated I_{CaL}, I_{to} and I_{Kur} channels in the full cell models.

Figure 1 shows uncertainty in parameter estimates for the I_{Na} channel current in the N model manifest in a range of possible outputs of the current trace in response to voltage steps. The medians of the posterior parameter distributions related to time constant behaviour were close to the original reported values but showed a high degree of uncertainty. This was the expected result as only steady-state data were used to calibrate I_{Na} of the N model. As a consequence, the time constant parameters in this example likely exhibit practical unidentifiability, as they cannot be constrained given the provided experimental data. It should be noted that the well-constrained parameter q_1 in Figure 1A is offset from the published value due to a constant offset applied to the steady-state curve in the N model justified by time- and/or temperature-dependent drifts in steady-state characteristics of the current [12].

In comparison, the C model used a more complete dataset to calibrate kinetics for this channel. Nevertheless, this model also exhibits parameters with high RSD values suggesting unidentifiability (Figure 2). In contrast to the practical unidentifiability observed in the case of the N I_{Na} model, this is likely due to structural identifiability issues. The high number of parameters in the C I_{Na} model (Figure 3D) facilitates over-fitting to experimental data and leads to redundancy of some parameters. In [4], Daly et al investigated the uncertainty in parameter estimates of the Hodgkin-Huxley AP model. They reported wide posteriors around the estimates of certain parameters in the potassium and sodium channels of that far simpler AP model. It therefore is unsurprising to observe these results in more complex models of a sodium channel where there is more opportunity for parameters to covary within the structure of the model. Additionally, the use of conventional voltage-clamp protocols further aggravates this issue as it only provides an indirect measure of the underlying gating kinetics [34].

We next re-calibrated the N and C models to the unified datasets. In Figure 2 it was apparent that the addition of data sources, most often relating to the time constant of gates, would reduce the uncertainty around the gating functions though often at the expense of increased uncertainty in other regions of the model behaviour. In the case of the N model of I_{Na}, the addition of time constant data led to a reduction in the RSD value of time constant parameters at the expense of increased RSD values of the steady-state parameters. This may be a result of the structure of the N model I_{Na}, with sigmoid functions for inactivation time constants, not providing a good fit to the experimental data. As a result, the ABC calibration reaches the sampling rate stopping criteria earlier because the steady-state experimental data now represents only a small portion of the overall calibration dataset.

The C model of I_{Na} has 29 parameters to constrain across three gates, the most of any of the channels investigated. Although using a complete dataset for calibration, the high RSD values of parameters show that this model still suffers from parameter unidentifiability. The complex form of the equations makes over-fitting possible when using conventional calibration processes such as simple least-squares, which would not highlight the consequences of doing so as with a Bayesian method such as ABC. Often these complex forms of equations are initially based on direct comparisons between the gating functions and the experimental data and may be tailored to the specific data sources selected for calibration, rather than through forward evaluations of the model. In [34], the authors highlight the importance of replicating the experimental conditions and voltage protocols as closely as possible when calibrating AP models, despite the inherent difficulties of doing so. The complex form of model gating functions, which are often combined in parallel, means that the behaviour of the gating function itself may not be representative of the behaviour of the full channel model when tested with experimental protocols.

Reducing the structural complexity of the model equations by adopting a standardised gating formulation showed channel-dependent success. For I_{Na}, the S formulation resulted in a significant reduction in RSD values for parameter posterior distributions ($p=0.02$ compared to N model, $p=0.04$ compared to C model) which suggests it is partly alleviating unidentifiability concerns. The I_{Na} S model output also gave a goodness-of-fit measure of converged residual lower than either other model (Figure 3D). Despite this, for some experiments the goodness-of-fit was clearly worse than either N or C model, such as for activation and slow recovery time constants. In addition, there was variability around the lower voltage range of the activation gate time constant for which there is an absence of experimental data, highlighting this model is not immune to practical identifiability issues. For I_{Na}, there appears to be an advantage to the less complex formulation which provides more confidence in the identifiability of

its parameters without sacrificing representation of the experimental data. Fewer parameters also allow more direct reasoning about the effects of altering gating parameters on the overall channel behaviour. As with any model, considerations should to be taken of the specific goals of the modelling study, though the S I_{Na} presents a less complex foundation from which to build on with additional, context-specific data.

For I_{CaL}, the S model produced approximately the same goodness-of-fit as the more complex N model. However, in this case, the similar RSD values across each model imply that the use of a simpler model structure did not alleviate issues relating to parameter unidentifiability. This is particularly noticeable in the steady-state activation gate of the channel, where there is a greater variation in the posterior behaviour compared to the other two models (Figure 4B). This is potentially a result of the way steady-state summary statistics are calculated through normalising to a reference value in the output. As a consequence, the gate is less constrained to be fully open at the maximum activation as the normalisation hides this behaviour. The unidentifiability of parameters across all models for this channel is likely a consequence of the relative paucity of experimental data relating to the voltage-dependent time constant behaviour of I_{CaL}, which has fewer voltages tested in the unified dataset compared to the other channels studied.

For both potassium channel models (I_{to} and I_{Kur}), simplifying the model structure is a balance between reduced unidentifiability of parameters and reduced goodness-of-fit to experimental data. The inactivation τ plot of Figure 5A shows an example where both the N and C models are able to capture the plateau region at upper voltages ranges while the S model tends to zero. Similarly, the form of the S model requires the peak of the time constant curve to occur at the mid-point of activation or inactivation which appears inappropriate for the activation gate of this channel. This is reflected in the higher converged residual of the S model compared to the N and C models (Figure 5B lower). The parameters of the less complex model have lower RSD values than the C model ($p < 0.001$) and a smaller range than the N model. This suggests that the closest fit of this model to the experimental data is identifiable, despite also being a poorer fit than either other model. This highlights the fact that low uncertainty in posterior parameters does not necessary imply a model fits the data well (and vice-versa), and a trade-off exists which may depend on the goals and particular use-case of a modelling study.

Beattie et al [16] used the same standardised gating formulation to model the behaviour of a rapid delayed rectifier potassium current using an information-rich voltage protocol. In their case, the studied current appears to satisfy the requirement of peak time constant of the gate at mid-point of the steady-state curve (see for example Figure 5 in [16]). Based on these observations and our results, this standardised approach may therefore be appropriate in cases when experimental data suggests particular requirements, such as this one, are met. Using a standard gating formulation alleviates problems associated with the high number of parameters in very detailed models, without sacrificing the biophysical basis for the model. In contrast to purely phenomenological models, the form of the S model is based on Eyring-derived transition rates giving its parameters a physical interpretation [19, 16].

The S model leads to a reduction in simulation times, which is an important consideration as patient-specific modelling is further explored in whole-heart tissue simulations. However, in contrast to simpler models which have been shown to reproduce patient-specific AP morphologies [35], the standardised formulation retains information about specific ion channel currents which provides a stronger body of evidence in terms of model validation. It would be encouraging if future ion channel modelling promoted the use of common forms of equations in cell models rather than the current heritage of complex equations. Another promising proposition is a model reductionist approach to reduce uncertainty in parameter estimates by eliminating parameters which have little effect on the model output, e.g. manifold boundary approximation [14].

When testing the new parameterisations in the full AP models, it was apparent that a proportion of samples led to non-physiological behaviour. This was also the case when combining samples from all new parameterisations, which generally caused simulations to fail. This highlights the importance of a feedback process in the development of AP models, where the form of the full AP also informs the design of the underlying currents. A future step for this work could follow a similar approach to Kernik et al. [36] with multiple stages of calibration. For example, the full AP samples in these results could be used to further constrain the posterior distribution of the channel model parameters by eliminating non-physiological cases. These results also demonstrate an important consideration in the development of full AP models that tends to be omitted from modelling papers: the sheer challenge and achievement of combining a variety of nonlinear models of individual channels usually developed in isolation into a single model of a cardiac cell and tuning to produce a physiological action potential.

Limitations. RSD was used as a measure of the width of parameter posterior distributions and as

an indicator of parameter unidentifiability in this study. This measure tends to become inflated when the mean value in the denominator is close to zero. This approach does not allow us to separate structural and practical unidentifiability and the likely form was inferred from the availability of experimental data and structural form of the model in experiments.

Our ABC stopping criterion for all experiments was set to halt execution once an iteration had dropped below a 1% particle acceptance rate. This was based on preliminary experiments on the C model where it was assumed the algorithm is close to the optimum solution once sampling became too difficult. However, in some cases this criterion may be excessive or insufficient, as was observed for example for the original N and S model of the I_{CaL} channel. Investigations into more appropriate stopping criterion were outside the scope of this work. Parameters involved in the calcium-dependent gate in I_{CaL} of all models were omitted from calibration and the gate set to a constant value due to the lack of specific data and difficulty in isolating calcium handling components of the cell model. Particularly for the C model, which relies on the calcium transient to modulate the inactivation rates, it is perhaps inappropriate to attempt calibration using this approach.

The calibration process relied on summary statistics of the model responses to the virtual voltage clamp protocols. Reducing the data in this fashion was necessary to obtain the same form as in the experimental dataset. However, as highlighted in [7], it is generally not possible to obtain a finite dimensional set of summary statistics that are sufficient to fully capture all relevant information obtained from a voltage clamp protocol.

Channel models with greater than 14 parameters (N: I_{CaL}, I_{Kur}; C: I_{Na}, I_{to}, I_{Kur}) could not be calibrated as a complete model due to the large number of particles required to sample the high-dimensional parameter hyperspace. In these cases, we calibrated the behaviour of parameter subsets for each gate separately to the relevant experimental data while leaving the remainder at their published values. It is possible that the original gates could affect the calibration of the chosen gate, for example in exponential fitting to decay traces for channels with fast and slow inactivation. Despite this, it should be noted that conventional calibration techniques (e.g. least squares regression) do not restrict the modeller from applying the method in the case of this kind of sparse sampling space and will not explicitly convey the implications of doing so.

Conclusions. In this work, we have applied ABC to re-calibrate the gating kinetics in detailed ion channel models of human atrial myocytes. We calibrated these models to the experimental datasets used in the published calibration and showed a portion of parameters exhibited wide posterior distributions indicative of unidentifiability. Calibration to more complete experimental datasets did not reduce the unidentifiability present, which suggested that it may be both structural and practical. Reducing the structural complexity of the model through a common gating form was successful in reducing unidentifiability in I_{Na} without sacrificing goodness-of-fit. Experiments with other channels suggested that a trade-off exists between tailoring a model to provide a good fit to experimental data, and identifiability of parameters as models become more complex. The technique employed in this work is general and could be applied to any model of an action potential.

Data access

Supplementary Material is available with the article. All code is available in the project repository at `https://github.com/charleshouston/ion-channel-ABC` under the human-atrial project. Results database files: Dryad doi:10.5061/dryad.p2ngf1vmc [37].

Author contributions

CH and CDC conceived of and designed the study and critically revised the manuscript. CH carried out the experiments and performed the data analysis. BM and LE carried out preliminary experiments and data analysis. CH drafted the manuscript. All authors gave final approval for publication and agree to be held accountable for the work performed therein.

Competing interests

The authors declare that they have no competing interests.

Funding

This work was supported by the British Heart Foundation [grant numbers PG/15/59/31621, RE/13/4/30184].

Acknowledgements

The authors would like to thank members of the ElectroCardioMaths programme of the Imperial Centre for Cardiac Engineering for discussions pertaining to this research.

References

[1] A. L. Hodgkin and A. F. Huxley, "A quantitative description of membrane current and its application to conduction and excitation in nerve," *The Journal of Physiology*, vol. 117, pp. 500–544, Aug. 1952.

[2] S. A. Niederer, M. Fink, D. Noble, and N. P. Smith, "A meta-analysis of cardiac electrophysiology computational models," *Experimental Physiology*, vol. 94, pp. 486–495, May 2009.

[3] G. R. Mirams, P. Pathmanathan, R. A. Gray, P. Challenor, and R. H. Clayton, "Uncertainty and variability in computational and mathematical models of cardiac physiology," *The Journal of Physiology*, vol. 594, no. 23, pp. 6833–6847, 2016.

[4] A. C. Daly, D. J. Gavaghan, C. Holmes, and J. Cooper, "Hodgkin-Huxley revisited: reparametrization and identifiability analysis of the classic action potential model with approximate Bayesian methods," *Royal Society Open Science*, vol. 2, p. 150499, Dec. 2015.

[5] R. H. Johnstone, E. T. Y. Chang, R. Bardenet, T. P. de Boer, D. J. Gavaghan, P. Pathmanathan, R. H. Clayton, and G. R. Mirams, "Uncertainty and variability in models of the cardiac action potential: Can we build trustworthy models?," *Journal of Molecular and Cellular Cardiology*, vol. 96, pp. 49–62, 2016.

[6] A. C. Daly, J. Cooper, D. J. Gavaghan, and C. Holmes, "Comparing two sequential Monte Carlo samplers for exact and approximate Bayesian inference on biological models," *Journal of the Royal Society, Interface*, vol. 14, no. 134, 2017.

[7] M. Sunnker, A. G. Busetto, E. Numminen, J. Corander, M. Foll, and C. Dessimoz, "Approximate Bayesian computation," *PLoS computational biology*, vol. 9, no. 1, p. e1002803, 2013.

[8] M. Fink, S. A. Niederer, E. M. Cherry, F. H. Fenton, J. T. Koivumki, G. Seemann, R. Thul, H. Zhang, F. B. Sachse, D. Beard, E. J. Crampin, and N. P. Smith, "Cardiac cell modelling: observations from the heart of the cardiac physiome project," *Progress in Biophysics and Molecular Biology*, vol. 104, pp. 2–21, Jan. 2011.

[9] D. Csercsik, K. M. Hangos, and G. Szederknyi, "Identifiability analysis and parameter estimation of a single HodgkinHuxley type voltage dependent ion channel under voltage step measurement conditions," *Neurocomputing*, vol. 77, pp. 178–188, Feb. 2012.

[10] A. A. Sher, K. Wang, A. Wathen, P. J. Maybank, G. R. Mirams, D. Abramson, D. Noble, and D. J. Gavaghan, "A local sensitivity analysis method for developing biological models with identifiable parameters: Application to cardiac ionic channel modelling," *Future Generation Computer Systems*, vol. 29, pp. 591–598, Feb. 2013.

[11] O. J. Walch and M. C. Eisenberg, "Parameter identifiability and identifiable combinations in generalized HodgkinHuxley models," *Neurocomputing*, vol. 199, pp. 137–143, July 2016.

[12] A. Nygren, C. Fiset, L. Firek, J. W. Clark, D. S. Lindblad, R. B. Clark, and W. R. Giles, "Mathematical model of an adult human atrial cell: the role of K+ currents in repolarization," *Circulation Research*, vol. 82, pp. 63–81, Jan. 1998.

[13] M. Courtemanche, R. J. Ramirez, and S. Nattel, "Ionic mechanisms underlying human atrial action potential properties: insights from a mathematical model," *The American Journal of Physiology*, vol. 275, no. 1, pp. H301–321, 1998.

[14] D. M. Lombardo and W.-J. Rappel, "Systematic reduction of a detailed atrial myocyte model," *Chaos: An Interdisciplinary Journal of Nonlinear Science*, vol. 27, p. 093914, Sept. 2017.

[15] K. H. Jger, S. Wall, and A. Tveito, "Detecting undetectables: Can conductances of action potential models be changed without appreciable change in the transmembrane potential?," *Chaos: An Interdisciplinary Journal of Nonlinear Science*, vol. 29, p. 073102, July 2019.

[16] K. A. Beattie, A. P. Hill, R. Bardenet, Y. Cui, J. I. Vandenberg, D. J. Gavaghan, T. P. de Boer, and G. R. Mirams, "Sinusoidal voltage protocols for rapid characterisation of ion channel kinetics," *The Journal of Physiology*, vol. 596, no. 10, pp. 1813–1828, 2018.

[17] D. S. Lindblad, C. R. Murphey, J. W. Clark, and W. R. Giles, "A model of the action potential and underlying membrane currents in a rabbit atrial cell," *American Journal of Physiology-Heart and Circulatory Physiology*, vol. 271, pp. H1666–H1696, Oct. 1996.

[18] C. H. Luo and Y. Rudy, "A dynamic model of the cardiac ventricular action potential. I. Simulations of ionic currents and concentration changes.," *Circulation Research*, vol. 74, pp. 1071–1096, June 1994.

[19] R. W. Tsien and D. Noble, "A transition state theory approach to the kinetics of conductance changes in excitable membranes," *The Journal of Membrane Biology*, vol. 1, pp. 248–273, Dec. 1969.

[20] J. Keener, J. Sneyd, S. S. Antman, J. E. Marsden, and L. Sirovich, eds., *Mathematical Physiology*, vol. 8/2 of *Interdisciplinary Applied Mathematics*. New York, NY: Springer New York, 2009.

[21] Y. Sakakibara, J. A. Wasserstrom, T. Furukawa, H. Jia, C. E. Arentzen, R. S. Hartz, and D. H. Singer, "Characterization of the sodium current in single human atrial myocytes," *Circulation Research*, vol. 71, pp. 535–546, Sept. 1992.

[22] M. Schneider, T. Proebstle, V. Hombach, A. Hannekum, and R. Rdel, "Characterization of the sodium currents in isolated human cardiocytes," *Pflugers Archiv: European Journal of Physiology*, vol. 428, pp. 84–90, Aug. 1994.

[23] T. Mewes and U. Ravens, "L-type Calcium Currents of Human Myocytes from Ventricle of Non-failing and Failing Hearts and from Atrium," *Journal of Molecular and Cellular Cardiology*, vol. 26, pp. 1307–1320, Oct. 1994.

[24] G. R. Li and S. Nattel, "Properties of human atrial ICa at physiological temperatures and relevance to action potential," *The American Journal of Physiology*, vol. 272, pp. H227–235, Jan. 1997.

[25] H. Sun, N. Leblanc, and S. Nattel, "Mechanisms of inactivation of L-type calcium channels in human atrial myocytes," *The American Journal of Physiology*, vol. 272, pp. H1625–1635, Apr. 1997.

[26] E. F. Shibata, T. Drury, H. Refsum, V. Aldrete, and W. Giles, "Contributions of a transient outward current to repolarization in human atrium," *American Journal of Physiology-Heart and Circulatory Physiology*, vol. 257, pp. H1773–H1781, Dec. 1989.

[27] Z. Wang, B. Fermini, and S. Nattel, "Sustained depolarization-induced outward current in human atrial myocytes. Evidence for a novel delayed rectifier K+ current similar to Kv1.5 cloned channel currents," *Circulation Research*, vol. 73, pp. 1061–1076, Dec. 1993.

[28] L. Firek and W. R. Giles, "Outward currents underlying repolarization in human atrial myocytes," *Cardiovascular Research*, vol. 30, pp. 31–38, July 1995.

[29] M. Clerx, K. A. Beattie, D. J. Gavaghan, and G. R. Mirams, "Four Ways to Fit an Ion Channel Model," *Biophysical Journal*, p. S0006349519306666, Aug. 2019.

[30] M. Clerx, P. Collins, E. de Lange, and P. G. A. Volders, "Myokit: A simple interface to cardiac cellular electrophysiology," *Progress in Biophysics and Molecular Biology*, vol. 120, pp. 100–114, Jan. 2016.

[31] E. Klinger, D. Rickert, and J. Hasenauer, "pyABC: distributed, likelihood-free inference," *Bioinformatics*, vol. 34, pp. 3591–3593, Oct. 2018.

[32] T. Toni, D. Welch, N. Strelkowa, A. Ipsen, and M. P. H. Stumpf, "Approximate Bayesian computation scheme for parameter inference and model selection in dynamical systems," *Journal of the Royal Society, Interface*, vol. 6, pp. 187–202, Feb. 2009.

[33] R. McElreath, *Statistical rethinking: A Bayesian course with examples in R and Stan*. Chapman and Hall/CRC, 2018.

[34] J. Carro, J. F. Rodrguez-Matas, V. Monasterio, and E. Pueyo, "Limitations in electrophysiological model development and validation caused by differences between simulations and experimental protocols," *Progress in Biophysics and Molecular Biology*, vol. 129, pp. 53–64, 2017.

[35] D. M. Lombardo, F. H. Fenton, S. M. Narayan, and W.-J. Rappel, "Comparison of Detailed and Simplified Models of Human Atrial Myocytes to Recapitulate Patient Specific Properties," *PLOS Computational Biology*, vol. 12, p. e1005060, Aug. 2016.

[36] D. C. Kernik, S. Morotti, H. Wu, P. Garg, H. J. Duff, J. Kurokawa, J. Jalife, J. C. Wu, E. Grandi, and C. E. Clancy, "A computational model of induced pluripotent stemcell derived cardiomyocytes incorporating experimental variability from multiple data sources," *The Journal of Physiology*, vol. 597, pp. 4533–4564, Sept. 2019.

[37] C. Houston, B. Marchand, L. Engelbert, and C. D. Cantwell, "Data from: Reducing complexity and unidentifiability when modelling human atrial cells," *Dryad, Dataset*, Dec. 2019.

arXiv:2001.10954v1 [q-bio.QM] 29 Jan 2020

Supplementary Material for: Reducing complexity and unidentifiability when modelling human atrial cells.

C. Houston[1,2], B. Marchand[2], L. Engelbert[2], C. D. Cantwell[1,2]

[1]ElectroCardioMaths Programme, Centre for Cardiac Engineering, Imperial College, London.
[2]Department of Aeronautics, Imperial College, London.

Contents

S1 Datasets and simulations **2**
S1.1 Data sources . . . 2
S1.2 Temperature adjustment . . . 3
S1.3 Voltage-clamp protocols and summary statistic functions . . . 5
S1.3.1 I_{Na} . . . 5
S1.3.2 I_{CaL} . . . 6
S1.3.3 I_{to} . . . 8
S1.3.4 I_{Kur} . . . 10

S2 Approximate Bayesian computation **12**

S3 Additional results **13**
S3.1 Gating functions for calibrations to original and unified datasets . . . 13
S3.2 I_{CaL} . . . 15
S3.3 I_{to} . . . 15
S3.4 I_{Kur} . . . 16
S3.5 Goodness-of-fit residuals . . . 17
S3.6 Action potential response . . . 18

S4 Model equations and numerical results **25**
S4.1 I_{Na} . . . 25
S4.2 I_{CaL} . . . 29
S4.3 I_{to} . . . 34
S4.4 I_{Kur} . . . 38

S1 Datasets and simulations

S1.1 Data sources

Table 1 contains a complete list of all experimental data sources for both original and unified datasets.

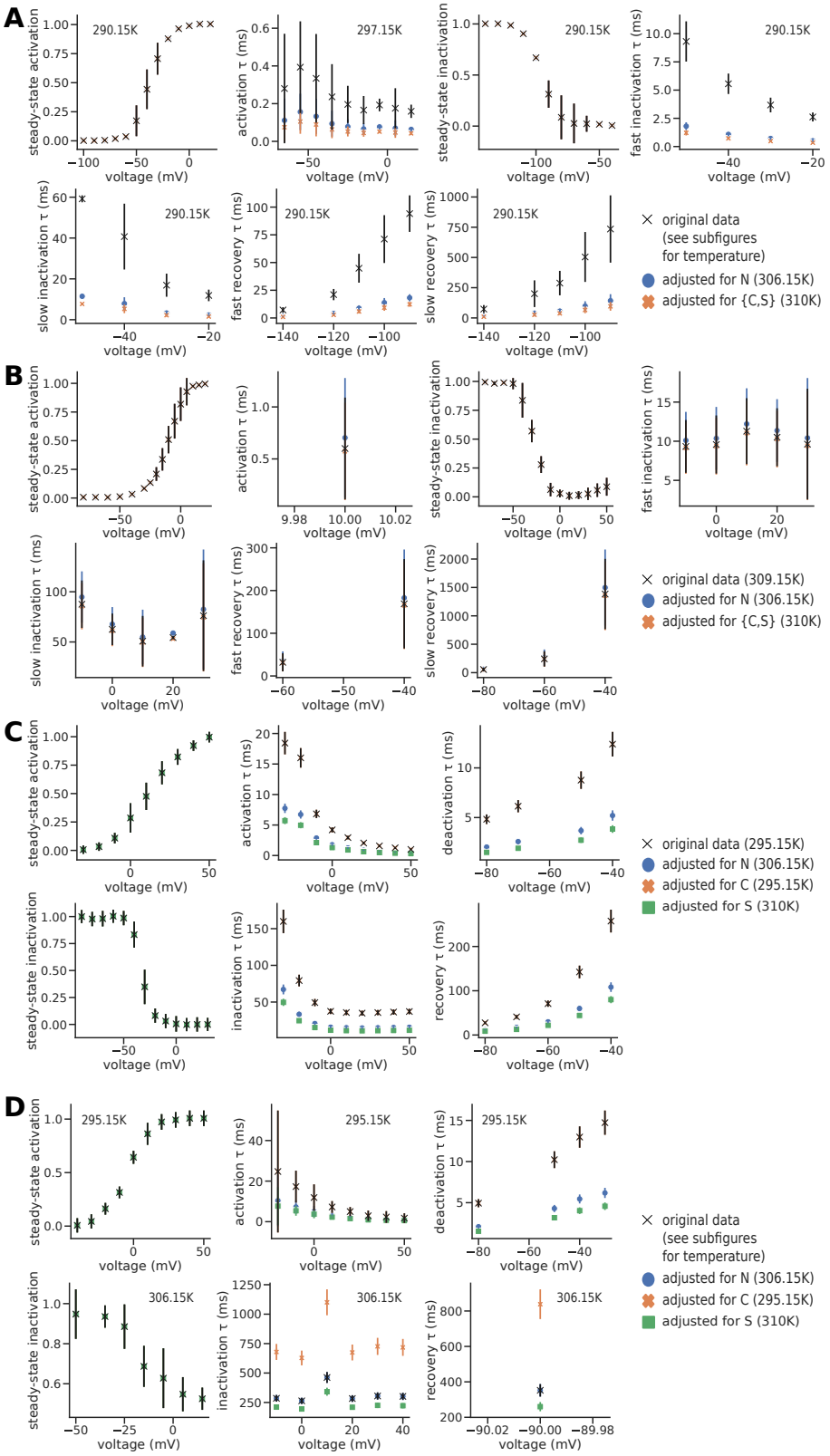
Channel	Gate		Data	N [1]	C [2]	Unified
I_{Na}	activation, m	m_∞	Fig. 2 [3]	✓	✓	✓
		τ_m	Fig. 3C [4]	✗	✓	✓
	inactivation*, $\{h, j\}$	$\{h, j\}_\infty$	Fig. 7 [3]	✓	✓	✓
		$\tau_{\{h,j\}}$ (inact.)	Fig. 5B [3]	✗	✓	✓
		$\tau_{\{h,j\}}$ (recov.)	Fig. 9 [3]	✗	✓	✓
I_{CaL}	activation, d	d_∞	Fig. 5C [5]^a Fig. 2B [6]^b	✓^{a}	✓^{b}	✓^{b}
		τ_d	Pg. H233 [6]	✗	✗	✓
	inactivation†, f	f_∞	Fig. 2B [6]	✓	✓	✓
		τ_f (inact.)	Fig. 3B [6]^a Fig. 4B [7]^b	✓^{a}	✓^{b}	✓^{a}
		τ_f (recov.)	Pg. H230 [6]	✓	✗	✓
I_{to}	activation, r	r_∞	Fig. 3A [8]^a Fig. 2A [9]^b	✓^{a}	✓^{b}	✓^{b}
		τ_r (act.)	Fig. 5D [2]‡	✗	✓	✓
		τ_r (deact.)	Fig. 5D [2]‡	✗	✓	✓
	inactivation, s	s_∞	Fig. 3C [10]^a Fig. 2C [9]^b	✓^{a}	✓^{b}	✓^{b}
		τ_s (inact.)	Fig. 4C [1]^{a,‡} Fig. 5D [2]^{b,‡}	✓^{a}	✓^{b}	✓^{b}
		τ_s (recov.)	Fig. 4C [1]^{a,‡} Fig. 5D [2]^{b,‡}	✓^{a}	✓^{b}	✓^{b}
I_{Kur}*	activation, a	a_∞	Fig. 8E [9]	✓	✓	✓
		τ_a (act.)	Fig. 8F [9]	✓	✓	✓
		τ_a (deact.)	Fig. 5B [2]‡	✗	✓	✓
	inactivation, i	i_∞	Fig. 3C [10]^{a,§} Fig. 7A [9]^{b,§}	✓^{a}	✓^{b}	✓^{a}
		τ_i (inact.)	Fig. 4D [1]^{a,‡} Fig. 5B [2]^{b,‡}	✓^{a}	✓^{b}	✓^{a}
		τ_i (recov.)	Fig. 4D [1]‡	✓	✗	✓

Supplementary Table 1: Summary of patch clamp experimental datasets used in modelling papers in human atrial myocytes for each channel studied. Ticks and crosses are used to indicate which datasets are included in the original model calibration and which compose the unified dataset. *There are some differences in the terminology used in each model. The N model refers to the inactivation gates of I_{Na} as h_1 and h_2, and the I_{Kur} channel as I_{sus}. †The L-type calcium current has a calcium-dependent inactivation process which is not calibrated in this experiment (discussed further in results). ‡In some cases it was not clear from the modelling paper where the comparison data plotted were obtained from. In these cases, the data points from the modelling paper itself are used and a protocol assumed based on the experimental paper cited. §In some cases it was not explicit which figure among a number of possibilities within a cited data source was used; the choice was inferred from the modelling paper.

S1.2 Temperature adjustment

The N model was created to simulate a human atrial action potential at 306.15K ($33°C$), whereas the C model was created to simulate at 310K ($\sim 37°C$). Time constant measurements of rise and decay rates are temperature-dependent, and thus it was important to account for this during the calibration. During ABC, time constant measurements from the experimental sources were adjusted to the temperature of the model being calibrated using a Q10 factor from an experimental source. The Q10 factors used are: I_{Na}: 2.79 [11]; I_{CaL}: 1.7 (activation), 1.3 (inactivation), both calculated from values in [6]; $I_{\{\mathrm{to,Kur}\}}$: 2.2 [9]. In the original publication for the C model, I_{to} and I_{Kur} were fitted at room temperature (295.15K) and then adjusted by the authors to the model temperature (310K) by dividing time constants by a factor of 3 [2]. To maintain consistency, we also calibrate the C model at room temperature rather than make any adjustment to the experimental data. The time constants for this channel are adjusted before being used to simulate a full action potential. The S model was always calibrated by adjusting experimental data to 310K. Figure 1 shows the temperature-adjusted datasets for all experiments across channel models.

When comparing channel models on the same figure throughout this work, their time constants are adjusted for the same temperature of 310K. For full action potential simulations, the N and C model time constants are kept at their model temperature, and only the S model time constant adjusted from 310K to 306.15K when it is added to the N model.



Supplementary Figure 1: Unified datasets for each channel model showing adjustments to experimental calibrating data at each model temperature. The adjustment is made using a Q10 factor as indicated in the text. **A** I_{Na}. **B** I_{CaL}. **C** I_{to}. **D** I_{Kur}.

S1.3 Voltage-clamp protocols and summary statistic functions

Throughout this section, the lettering in the headers refers to the figure describing voltage protocols for the channel. All curve fitting for finding time constants was carried out using the *scipy.optimize* Python library.

S1.3.1 I_{Na}

All experiments by Sakakibara et al. [3] used equal extracellular and pipette solution sodium concentration of 5mM at a temperature of 290K ($17°C$). The time constant of activation experiment from Schneider et al. [4] used sodium concentration of 120mM in the extracellular solution and 70mM in the pipette solution, and the experiment was conducted at 297K ($24°C$).

A: Steady-state activation (p.538 [3]). The standard protocol to measure steady-state activation of the channel holds the membrane at a sub-threshold potential of -140mV and then steps the channel to a series of voltage steps between -100mV and 20mV, with intervals of 10mV. The steps last for 1s and there are 10s between each step.

The degree of steady-state activation is measured by recording the peak current during the voltage step (normalised to cell capacitance). The conductance is calculated by dividing the peak current by the forcing term, usually assumed to be the potential difference to the Nernst potential of the primary ion carrier, $g = \frac{I}{V - E_{\mathrm{X}}}$. In the computational protocols, we directly measure the conductance of the channel to bypass this calculation. To plot the activation curve, the conductance is plotted against the voltage step normalised to its maximum value in any voltage step.

B: Time constant of activation (p.85 [4]). The time constant constant of inactivation is measured by fitting an equation to the current trace from a standard steady-state activation protocol as described in the previous protocol. In this case, the holding potential is -135mV and the steps are from -65mV and 15mV in steps of 10mV. The time at holding potential between each step was not given and so assumed to be 10s (more than enough for the I_{Na} channel to return to steady-state) and each test pulse lasted for 12ms.

The activation time constant was measured by fitting the entire current trace at a pulse to the equation $I_{\mathrm{Na}} = I_{\mathrm{Na,max}} \left[1 - e^{-t/\tau_{\mathrm{m}}}\right]^3 e^{-t/\tau_{\mathrm{h}}} + \text{constant}$ (p.87 [4]). In this equation, t is the time in ms, $I_{\mathrm{Na,max}}$ is the peak of the current trace, τ_{m} is the activation time constant and τ_{h} is the inactivation time constant.

C: Steady-state inactivation (p.541 [3]). The protocol used to measure steady-state inactivation is often also referred to as an availability protocol. The membrane is held at a holding potential of -140mV for 10s, then stepped to a conditioning potential for 1s to activate and inactivate the channel. The membrane potential is returned to the holding potential for 2ms before stepping to a test pulse at -20mV for 30ms. A series of different conditioning pulses between -140mV and -40mV in steps of 10mV is used to test the amount of inactivation of the channel at different voltages.

The steady-state inactivation is measured by recording the peak current during the test pulse, normalised to the current in a test pulse when no conditioning step is applied (usually the maximum current amplitude). In the virtual voltage clamp experiment, we measure conductance directly in this step (which is equivalent as the forcing is the same during each test pulse and eliminated during the normalisation).

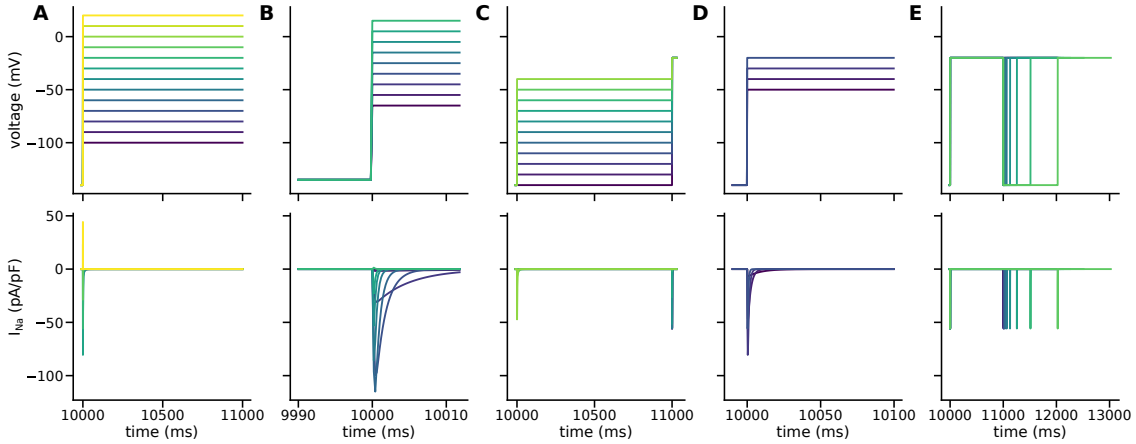
D: Fast/slow inactivation time constant (p.539 [3]). The protocol to determine inactivation time constants is a simple steptrain of test pulses from a holding potential of -140mV for 10s to a series of 100ms test pulses to voltages from -50mV to -20mV in steps of 10mV.

The fast and slow inactivation constants are determined by fitting the *decay* part of the current trace (after the peak current) to the equation $I_{\mathrm{Na}} = A_1 e^{-t/\tau_{\mathrm{f}}} + A_2 e^{-t/\tau_{\mathrm{s}}} + A_0$ (p.538 [3]) where A are amplitude variables, t is the time and τ_{f} and τ_{s} are the fast and slow time constants of inactivation respectively.

E: Fast/slow recovery time constant (p.538 [3]). The time constants of recovery from inactivation were determined using a double pulse protocol. The first pulse is a conditioning pulse for 1000ms to -20mV followed by a recovery period to a holding potential between -140mV and -90mV in steps of 10mV, of varying length between $2 - 1000$ms (this was not specified and we assumed a series of $t_{\mathrm{r}} = 2^i$ where $i = 1, 2...10$). The recovery period is followed by a test pulse identical to the conditioning pulse. We assumed 10s at holding potential between each pair of pulses.

The recovery time constant is measured through a series of processing steps. Firstly, the peak current in the test pulse is normalised to the peak current in the preceding conditioning pulse to give a measurement of proportion of the channel recovery for each recovery time period. This recovery measure is plotted against the recovery time period and the resulting curve is fit to a double exponential equation $r = A_0 - A_1 e^{-t_{\mathrm{r}}/\tau_{\mathrm{r(f)}}} - A_2 e^{-t_{\mathrm{r}}/\tau_{\mathrm{r(s)}}}$ where r is the proportion of recovery, A are amplitude parameters, t

is the recovery time period and $\tau_{r(f)}$ and $\tau_{r(s)}$ are the fast and slow recovery time constants respectively. These values are calculated for each holding potential.



Supplementary Figure 2: Voltage steps and current response (from C model) of I_{Na} protocols. A: steady-state activation, B: time constant of activation, C: steady-state inactivation, D: fast and slow time constants of inactivation, E: fast and slow time constants of recovery from inactivation. The recovery protocol is repeated at multiple holding potentials (only one shown). See text for details of how the current traces are processed into summary statistics.

S1.3.2 I_{CaL}

Experiments by Mewes and Ravens [5] were carried out at room temperature (assumed by authors to be 295K) and external solution with calcium concentration of 1.8mM. Those by Li and Nattel [6] were conducted at 309K with 2.0mM external calcium concentration. Experiments by Sun et al. [7] were completed at room temperature (assumed by authors to be 296K) and external calcium concentration of 1mM. It is difficult to estimate the level of intracellular calcium concentration during these experiments due to the mechanisms of the intracellular calcium stores and buffering. In our virtual voltage clamp experiments, the level of the intracellular calcium was kept constant at the resting value from the published N and C models (72.5nM and 101.3nM respectively) and, for the S model, set to the same value as the C model (101.3nM).

A, B: Steady-state activation (p.1309 [5], p.H228 [6]). In Mewes and Ravens [5], steady-state activation was assessed using a conventional steptrain protocol from a holding potential of −40mV to 450ms steps between −35mV to 15mV in intervals of 5mV, with 10s between each pulse. In Li and Nattel [6], the activation curve was generated from the IV curve dataset which used a similar step train protocol. This time the holding potential was −80mV and the 300ms test pulses ranged from −80mV to 20mV in steps of 10mV. Both activation curves were generated as described in I_{Na} steady-state activation.

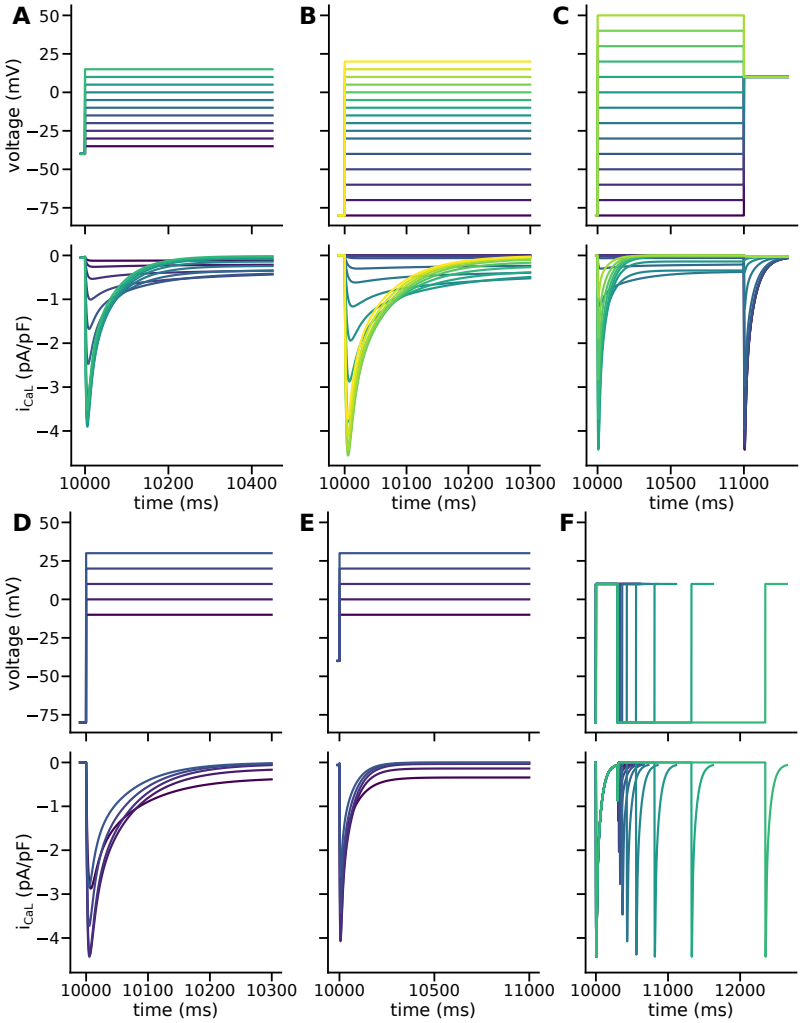
B: Activation time constant (p.H233 [6]). The single activation time constant value was determined from the current trace evoked during the 10mV test pulse in the activation protocol from [6]. The activation time constant was estimated by fitting the upstroke of the normalised current trace to $I_{CaL} = 1 - Ae^{-t/\tau_a}$ where A is an amplitude parameter, t is the time and τ_a is the activation time constant.

C: Steady-state voltage-dependent inactivation (p.H229 [6]). The voltage-dependent steady-state inactivation was assessed using a standard availability protocol. Conditioning pulses to a series of voltages between −80mV and 50mV in steps of 10mV were followed immediately by a test pulse to 10mV for 300ms. In [6], there are three datasets using different length of conditioning pulses of either 150ms, 300ms or 1000ms. We use the 1000ms prepulse dataset as this was used for calibration in both modelling papers. The inactivation curve was calculated as in I_{Na} steady-state inactivation.

D, E: Fast/slow voltage-dependent inactivation time constant (p.H229-H230 [6], p.H1628 [7]). Fast and slow inactivation time constants were calculated by fitting a biexponential equation to the decay portion of the current trace during test pulses from a holding potential. In [6], three different holding potentials were used and we use the same as the modelling papers: −80mV. Test pulses lasted 300ms

to steps between −10mV and 30mV in intervals of 10mV (we assume 10s between pulses). In [7], the holding potential was −80mV, test pulses had duration 1000ms with the same levels as above, and were preceded by a 500ms pulse to −40mV. In both cases, time constants of inactivation were calculated by fitting the decay portion of the current trace during the test pulses to $I_{\mathrm{CaL}} = A_0 + A_f e^{-t/\tau_{\mathrm{f}}} + A_s e^{-t/\tau_{\mathrm{s}}}$ were A are amplitude parameters, t is the time and τ_{f} and τ_{s} are the fast and slow time constants respectively.

F: Fast/slow voltage-dependent recovery time constant (p.H229-H230 [6]). Recovery time constants were assessed with a two-pulse protocol as in I_{Na} recovery experiments. In this case, the holding potentials were −80mV, −60mV and −40mV with conditioning and test pulses both to 10mV for 300ms. Recovery periods were generated from $t_{\mathrm{r}} = 2^i$ where $i = 1, 2, ..., 11$ based on the range of data points in Fig 4B [6]. The data was processed as in I_{Na} recovery experiments with the exception that a single exponential function was used to fit the −80mV recovery curve to give a single (slow) recovery time constant.



Supplementary Figure 3: Voltage steps and current response (from N model) of I_{CaL} protocols. A: steady-state activation [5], B: steady-state and time constant of activation [6], C:steady-state inactivation [6], D: fast and slow time constants of inactivation [6], E: fast and slow time constants of inactivation [7], F: fast and slow time constants of recovery from inactivation [6]. The recovery protocol is repeated at multiple holding potentials (only one shown). See text for details of how the current traces are processed into summary statistics.

S1.3.3 I_{to}

Experiments by Shibata et al. [8] and Wang et al. [9] were conducted at room temperature (assumed to be 295K). Firek and Giles [10] used temperature of 306K ($33°C$). Shibata et al. used an extracellular and pipette potassium concentration of 4.5mM and 150mM respectively, Wang et al. used 5.4mM and 130mM and Firek et al. used 5.4mM and 140mM.

Some data for I_{to} was extracted directly from the N and C modelling papers [1, 2] as the source of the comparison experimental data plotted was not clear from the text. In these cases, conditions were assumed to be the same as the lab which produced the model. Thus, conditions for the assumed experimental data from Nygren et al. [1] was set to the same conditions as Firek and Giles [10] above, and data from Courtemanche et al. [2] was assumed to have been collected at the conditions in Wang et al. [9].

A, B: Steady-state activation (p. H1776 [8], p.1065 [9]). In Shibata et al. [8], steady-state activation was determined by holding at a potential of −60mV for 20s, then depolarising for 15ms to a step between −30mV to 80mV, and finally stepping to −40mV for 100ms. The activation curve was generated by recording the peak current amplitude in the final step (the 'tail' current). Wang et al. [9] used a standard steady-state activation protocol with a holding potential of −80mV to a series of test potentials between −40mV and 50mV and measured the peak current during the 1000ms depolarising step (before processing as above for I_{Na}).

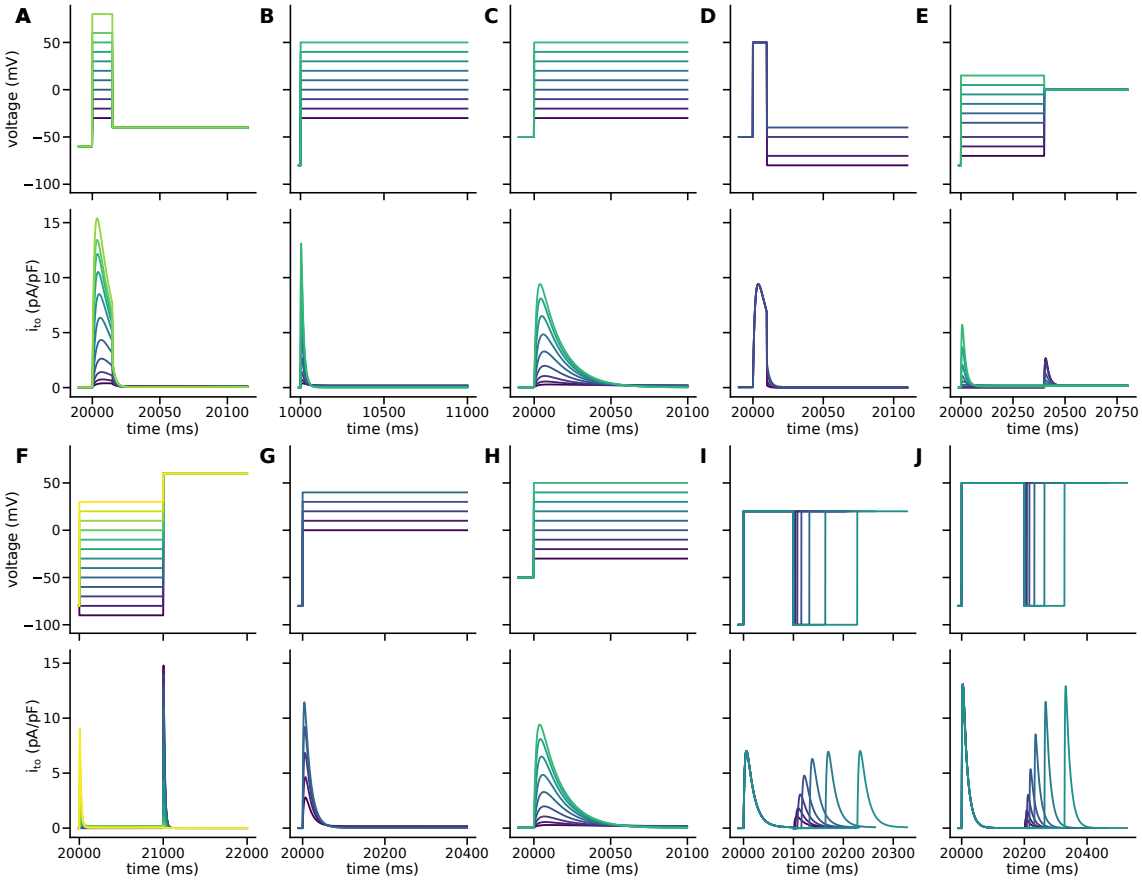
C: Activation time constant (p.H305 [2]). Activation time constant data corresponding to that plotted in the modelling paper could not be found in the cited experimental source [9]. A simple steptrain protocol as described in [9] was assumed with a holding potential of −50mV and 100ms test pulses. The activaton time course of I_{to} was fitted to a single exponential equation: $I_{\text{to}} = A_0 - Ae^{-t/\tau_{\text{a}}}$ where A parameters are amplitudes, t is the time course and τ_{a} is the activation time constant.

D: Deactivation time constant (p.H305 [2]). The deactivation time constant data source is also uncertain and it is assumed to use a similar protocol as in Fig. 9A in Wang et al. [9]. This protocol holds the membrane potential at −50mV for 20s before applying a 10ms conditioning pulse to 50mV. This is followed by a test pulse to elicit a tail current, which is fit to a single exponential (same as the activation time constant above) to determine the deactivation time constant.

E, F: Steady-state inactivation (p.34 [10], p.1065 [9]). In Firek and Giles, a standard steady-state availability protocol was applied as described in more detail in I_{Na} steady-state inactivation. The holding potential is −80mV, followed by a 400ms conditioning pulse to levels between −80mV and 16mV, and finally a 400ms test pulse to 0mV to activate the outward current. Wang et al. [9] similarly uses a standard availability protocol with the same holding potential followed by 1000ms conditioning pulse to a range of voltages between −90mV and 30mV followed by a 1000ms test pulse to 60mV. Output was processed into summary statistics as described in I_{Na} steady-state inactivation.

G, H: Inactivation time constant (p.66 [1], p.H305 [2]). It was not clear in either N or C model where experimental comparison data of time constants of inactivation for I_{to} were obtained from. Consequently, simple protocols were assumed based on single-pulse protocols in experimental papers originating from the same labs. For [1], a single pulse protocol from a holding potential of −80mV to 400ms test pulses between 0mV and 40mV was applied and the decay phase of the current trace fit to a single exponential equation as above for activation time constants. For [2], a similar protocol was assumed based on [9] with a holding potential of −50mV and 100ms test pulses to between −40mV and 50mV.

I, J: Recovery time constant (p.66 [1], p.H305 [2]). Similarly to the inactivation time constant data, it was unclear where the recovery data was obtained from for both N and C models. For the N model, we assume the recovery protocol in [8] was used. This is a standard two-pulse recovery protocol with holding potentials of −100mV, −80mV and −60mv and 100ms test pulses to 20mV. For the C model, we assume the protocol in [9] was used with holding potential between −60mV and 40mV and 200ms test pulses to 50mV.



Supplementary Figure 4: Voltage steps and current response (from N model) of all I_{to} protocols. From left to right: A: steady-state activation [8], B: steady-state activation [9], C: activation time constants [2], D: deactivation time constants [2], E: steady-state inactivation [10], F: steady-state inactivation [9], G: time constant of inactivation [1], H: time constant of inactivation [2], I: time constant of recovery from inactivation [1], J: time constant of recovery from inactivation [2]. The recovery protocols are repeated at multiple holding potentials (only one shown for each). See text for details of how the current traces are processed into summary statistics.

S1.3.4 I_{Kur}

Experiments by Wang et al. [9] and Firek and Giles [10] use the same conditions stated above for I_{to}. As before, in some cases it was unclear where the comparison data in the modelling papers was obtained from. Details are given in the following sections.

A: Steady-state activation, activation time constant (p.1069 [9]). I_{Kur} was measured from a holding potential of −50mV followed by a 1s prepulse to 50mV (experimentally used to inactivate the I_{to} current which would otherwise interfere with isolating I_{Kur}). The potential is returned to −50mV for 20ms before being stepped to a range of 100ms test pulses between −40mV to 50mV each followed by a repolarising pulse to −10mV. I_{Kur} was measured as the peak current in the final repolarising pulse and the activation curve determined as previously described for I_{Na} steady-state activation. The activation time constants were determined by fitting the time course of I_{Kur} trace during the test pulses to a single exponential function as described above.

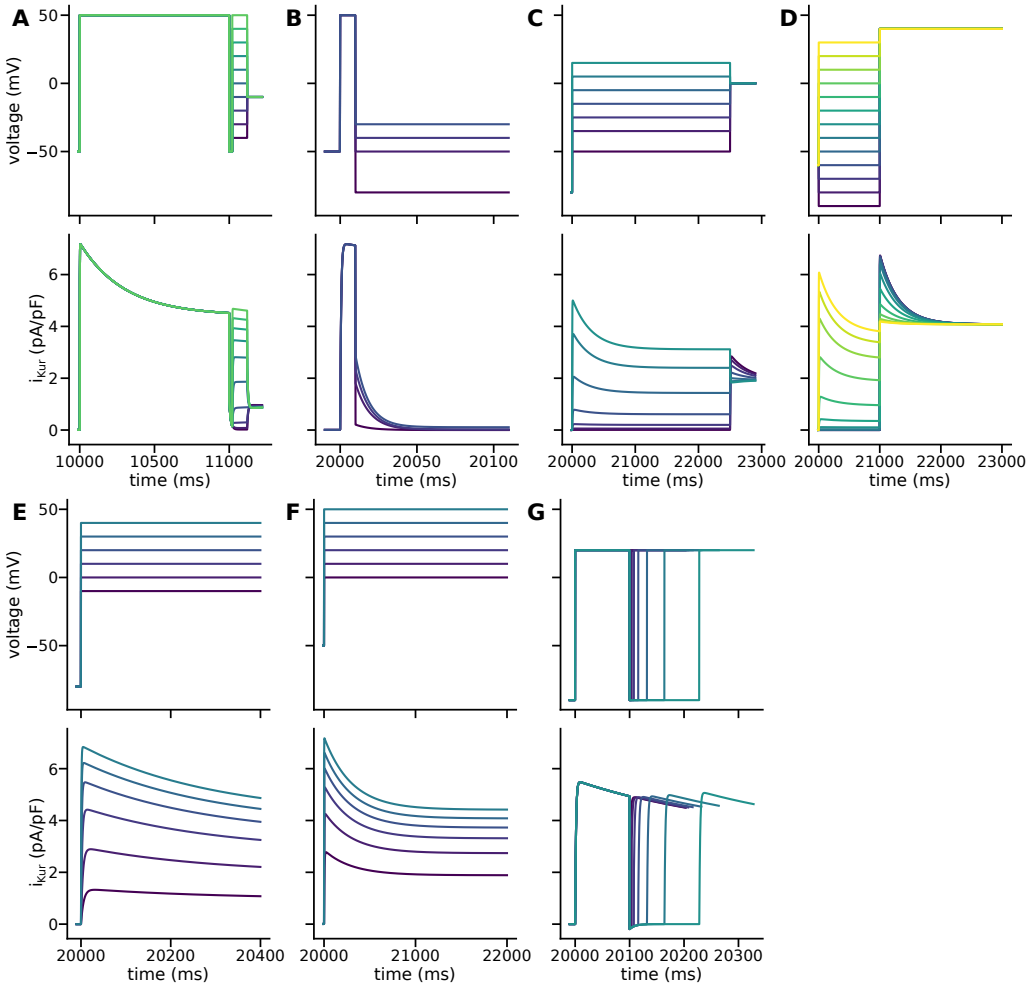
B: Deactivation time constant (p.305 [2]). As it was not clear where the data points were obtained from, the protocol from Fig. 9 in [9] was assumed to have been used. This is the same protocol as described in deactivation time constant for I_{to}.

C, D: Steady-state inactivation (p.34 [10], p.1068 [9]). For Firek and Giles [10], the protocol was the same as the steady-state inactivation protocol described for steady-state inactivation of I_{to} with an increase of the length of the conditioning pulse from 400ms to 2500ms. I_{Kur} was measured as the steady-state current at the end of the test pulse. In Wang et al. [9], steady-state inactivation is measured from the steady-state current at the end of a 2000ms test pulse to 40mV after a 1000ms conditioning pulse from a range of voltages. The holding potential was −60mV.

E, F: Inactivation time constant (p.66 [1], p.H305 [2]). It was unclear where the experimental data points from the N model paper came from. We assume they are generated from the protocol used in [10] from the same lab. This protocol is a simple 400ms step to a range of potentials from a holding potential of −80mV. In [10], the current decay is fit to a double exponential equation in order to separate I_{to} and I_{Kur} decay rates. As in the virtual voltage clamp there is only I_{Kur}, we fit the current decay to a single exponential.

Similary for the C model, we assume a similar protocol as in [9] was used. This is a simple 2000ms step to a range of test potentials from a holding potential of −50mV. The decay portion of the current trace is fit to a single exponential function as above.

G: Recovery time constant (p.66 [1]). As previously for I_{to}, we assume that the recovery protocol from [8] was used to determine a recovery time constant for I_{Kur}. The protocol is as described for I_{to} recovery time constant.



Supplementary Figure 5: Voltage steps and current response (from N model) of all I_{Kur} protocols. A: steady-state activation and activation time constant [9], B: deactivation time constants [2], C: steady-state inactivation [10], D: steady-state inactivation [9], E: time constant of inactivation [1], F: time constant of inactivation [2], G: time constant of recovery from inactivation [1]. See text for details of how the current traces are processed into summary statistics.

S2 Approximate Bayesian computation

Formally, ABC approximates the true parameter posterior distribution $P(\boldsymbol{\lambda}|\boldsymbol{D})$ by $P(\boldsymbol{\lambda}|\rho(\hat{\boldsymbol{D}}, \boldsymbol{D}) \leq \epsilon)$ where $\boldsymbol{D}$ are the experimental data, ρ is the chosen distance function, $\hat{\boldsymbol{D}}$ is the model summary statistics and ϵ is the threshold value. We use the Toni ABC sampler based on sequential Monte Carlo to infer our parameter posterior distributions [12]. In this sampler, the ABC process above is repeated through a number of iterations with reducing ϵ. A population of parameter samples, referred to as 'particles', are propagated through each iteration and represent a discrete surrogate to the continuous posterior distribution.

At each iteration of the algorithm, the previous population of particles are perturbed slightly, by a multivariate Gaussian kernel, and used as the prior distribution for the current iteration. ϵ is reduced over iterations and chosen as the median distance of samples from the previous iteration. The particle population number is set according to the number of parameters being constrained in the experiment by considering the size of the parameter sampling hyperspace and assuming at least two particles in each dimension. A limit of 10000 particles is enforced due to computational demands. The algorithm terminates when less than 1% of parameter samples are accepted in a given iteration indicating the algorithm is struggling to improve on the current optimum. This criterion is chosen over termination at an absolute value of the distance metric termination used in other studies due to differences in number of model parameters and availability of data between experiments.

To compare our model summary statistics to the experimental data (which include error measurements at each point), we use a weighted Euclidean distance function

$$\rho(\hat{\boldsymbol{D}}, \boldsymbol{D}) = \left[\sum_{i=0}^{M} \left(\frac{\hat{D}_i - D_i}{w_i} \right)^2 \right]^{1/2}, \tag{1}$$
$$w_i = \max(\sigma_i, \delta)\, n_{\mathrm{exp}|i},$$

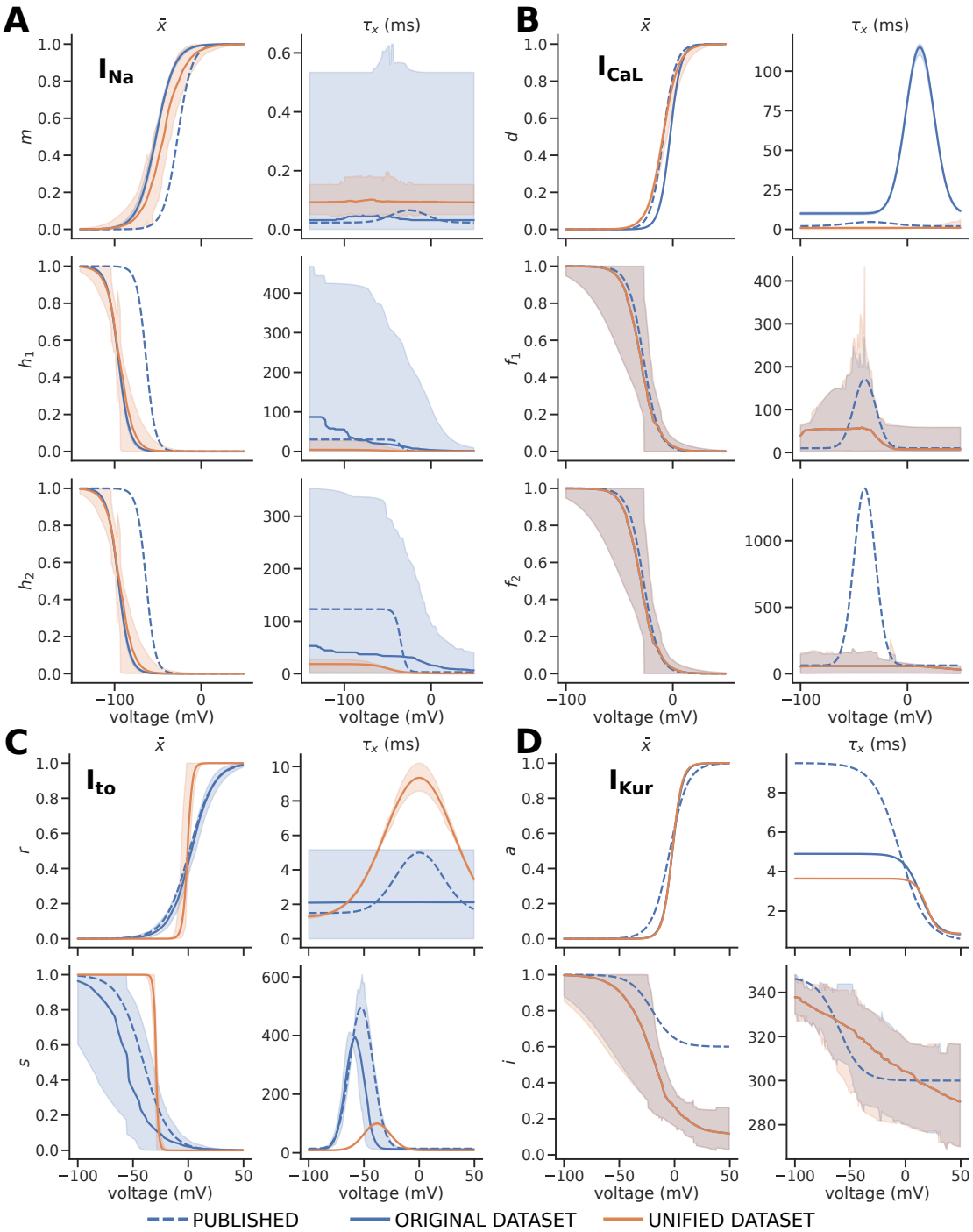
where w_i are the weights for each data point, σ_i is the standard deviation associated with the error at each data point, δ is a regularisation factor applied when weights are close to zero, and $n_{\mathrm{exp}|i}$ is the number of data points within the experiment. In this work δ was set to 0.05. Once generated, the weights are also mean-normalised to improve convergence of the ABC algorithm. The choice of distance function reduces the weighting of data points based on the magnitude of experimental uncertainty. This allows us to use information of which experimental data points we are relatively more confident about during the model calibration, propagating some of the experimental uncertainties through to this stage in the model development [13]. In some cases for I_{to} and I_{Kur}, it was not clear in the modelling paper where the data were obtained. In these cases, the points displayed in the figure from the modelling paper were digitised and 10% standard deviation error assumed (based on the error of similar measurements given in [9]).

Additionally, we account for the fact that we are simultaneously calibrating to multiple datasets by weighting according to the number of data points in a specific experiment. This provides balance between the different types of channel behaviour, rather than favouring an experiment with a greater number of data points. Each dataset is normalised to the maximum value in that experiment to avoid preference towards datasets with measurements at a larger scale in the ABC loss function.

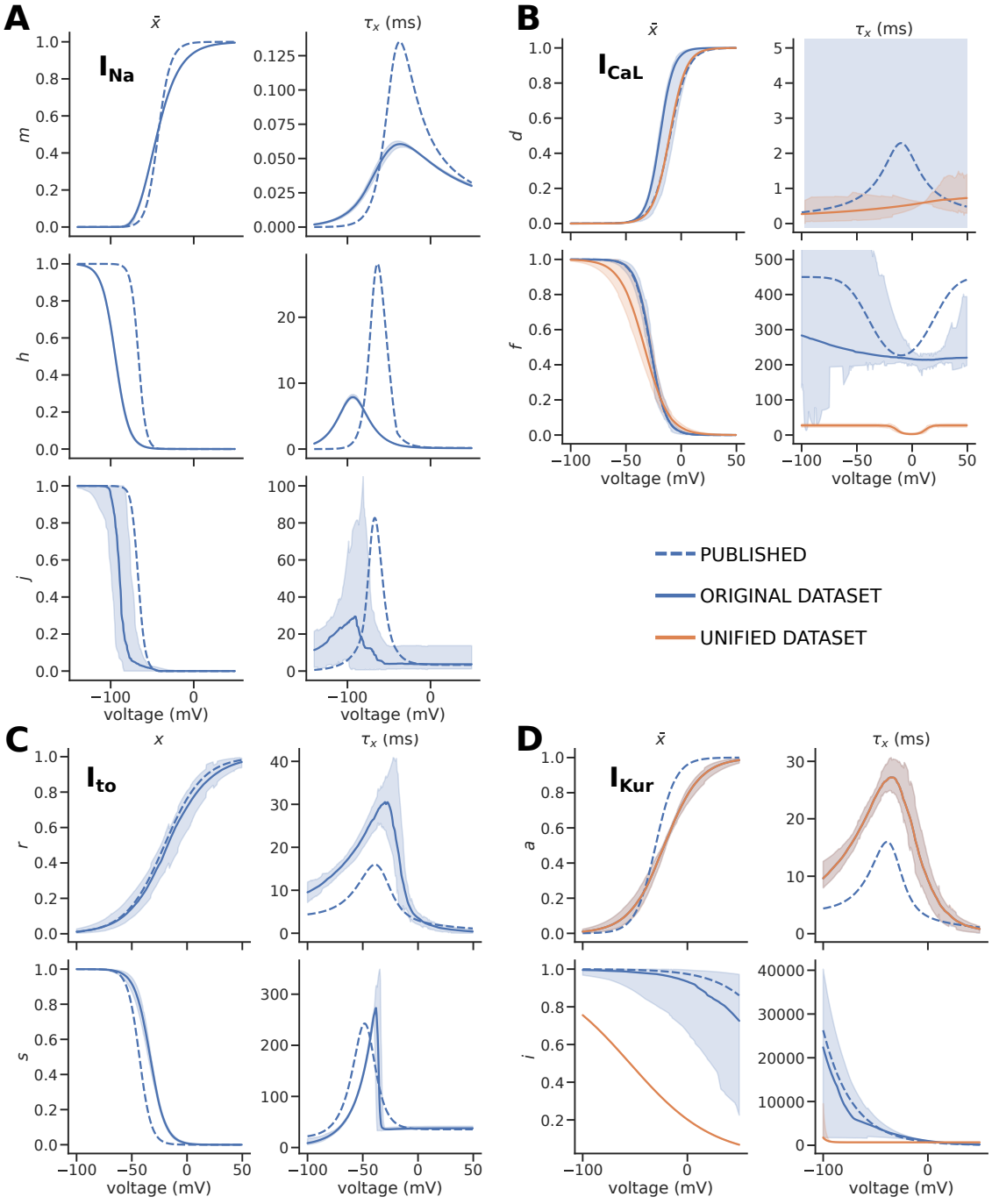
A uniform prior distribution is used for each model parameter in the first iteration. The width of this prior is set to be sufficiently wide to cover the range of physiological possibilities. After convergence, the parameter posterior distributions are inspected and, if observed to be restricted by the lower or upper limit of the prior, the calibration is re-started with a wider prior. For the S model, prior ranges are set as in [14].

S3 Additional results

S3.1 Gating functions for calibrations to original and unified datasets

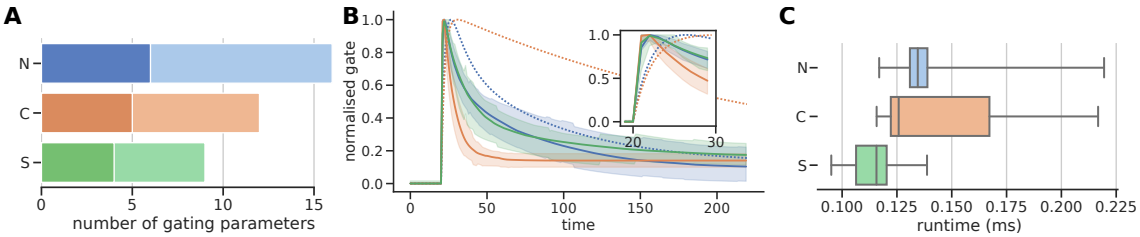


Supplementary Figure 6: A-D Steady-state and time constant functions for each channel of the N model using original calibration dataset and unified dataset. Blue refers to original dataset and orange to unified dataset. Data displayed as median line with shading representing 89% HDPI of 100 samples from the parameter posterior distribution.



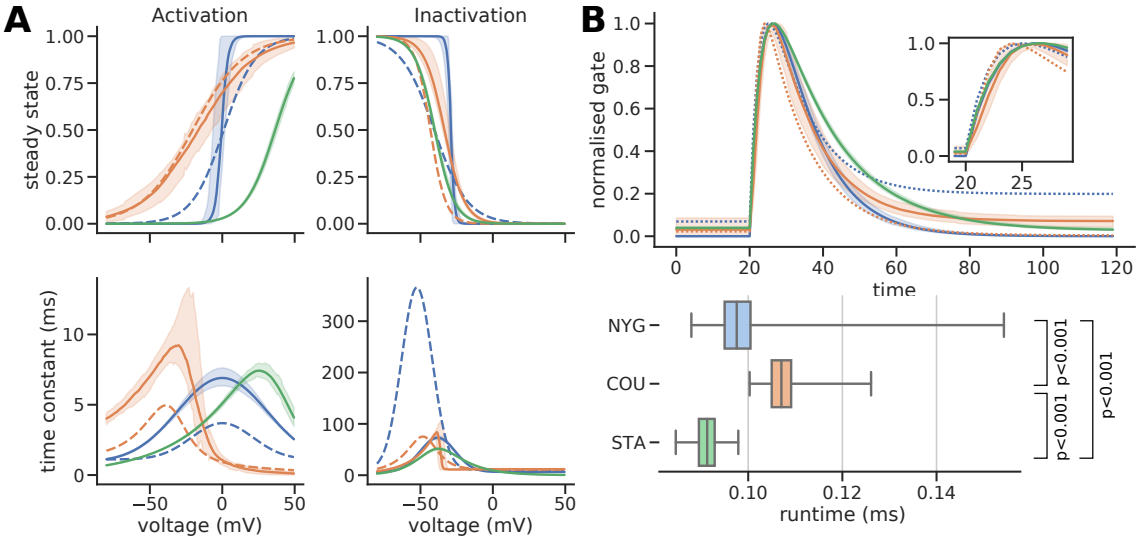
Supplementary Figure 7: A-D Steady-state and time constant functions for each channel of the C model using original calibration dataset and unified dataset. Blue refers to original dataset and orange to unified dataset. Data displayed as median line with shading representing 89% HDPI of 100 samples from the parameter posterior distribution. Note for I_{Na} and I_{to} the original and unified dataset are the same.

S3.2 I_{CaL}



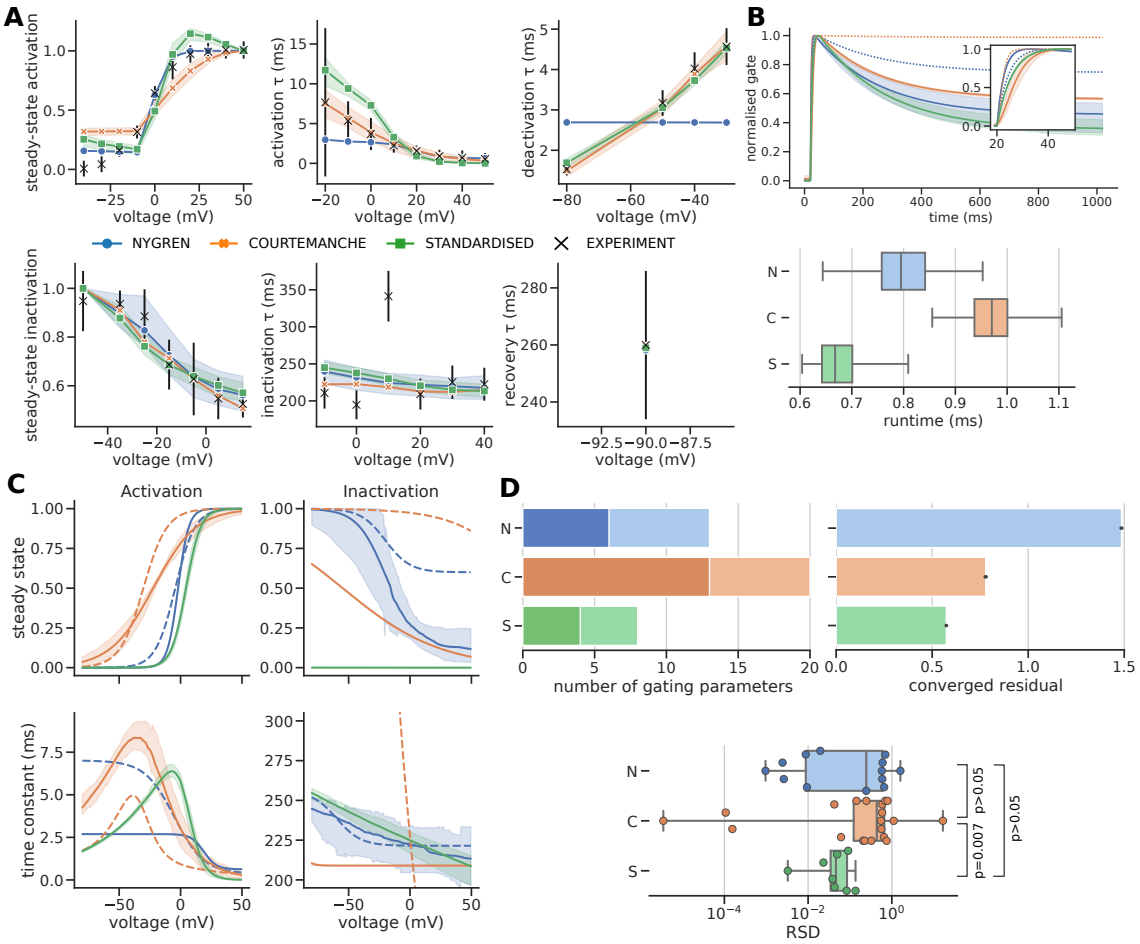
Supplementary Figure 8: **A** Number of gating parameters in equations for each I_{CaL} model, separated into activation (dark) and inactivation (light). **B** Example traces from each model generated from the last step of a train of 100 steps from -80 mV to -10 mV for 200 ms at a rate of 1 Hz using 100 samples from the parameter posterior distributions. Higher detail of the activation portion of the trace is shown in the inset plot. Output is summarised as median line with shading representing 89% HDPI. Dashed lines indicate the response of the published N and C models. **C** Boxplot comparing runtime of the simulation to generate each trace in B for each model.

S3.3 I_{to}



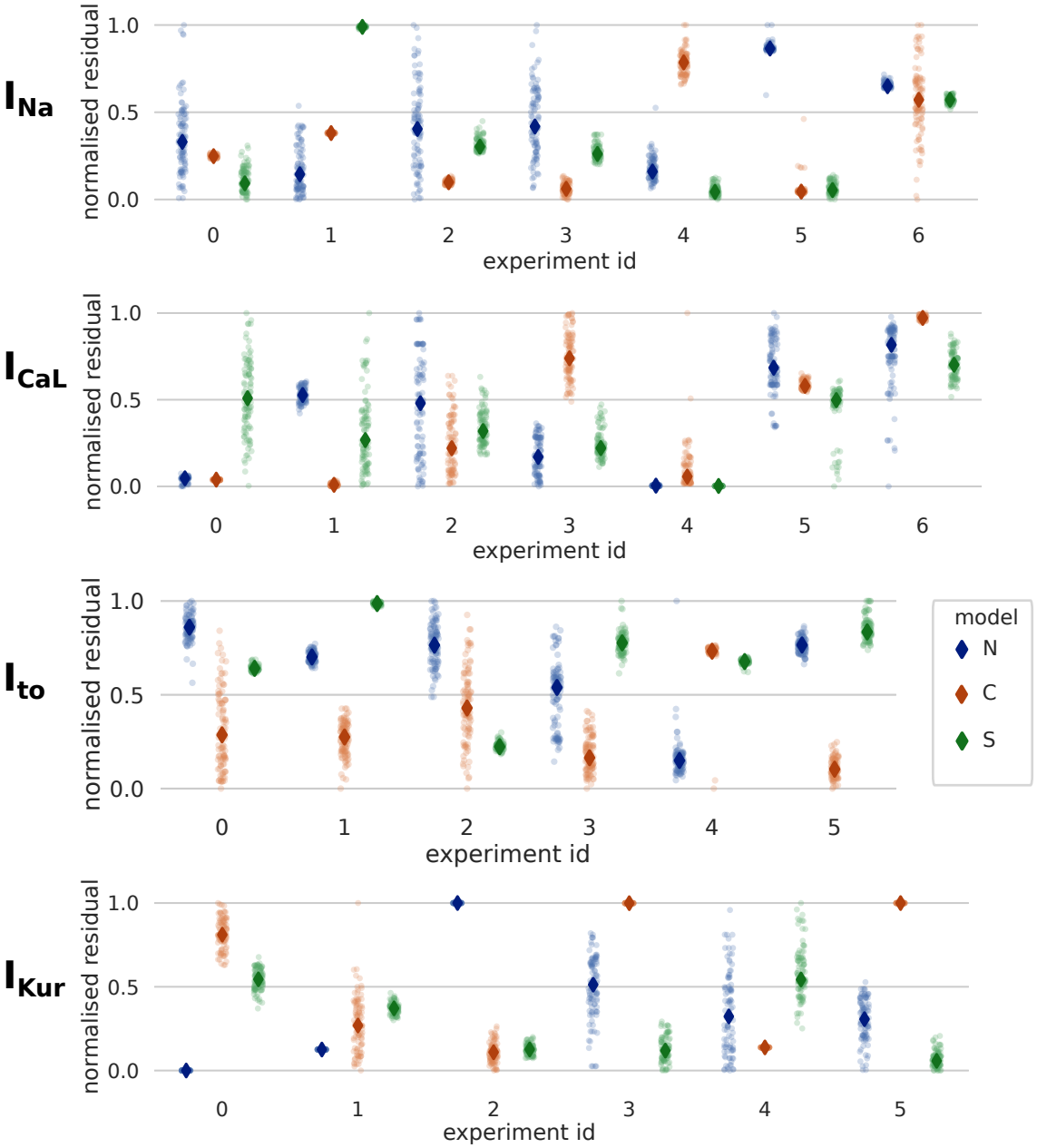
Supplementary Figure 9: **A** Steady-state and time constant functions for I_{to} model. Plotted as median line with shading indicated 89% HDPI from 100 samples from the parameter posterior distribution. Dashed lines indicate the published values. **B** Example traces from each model generated from the last step of a pulse train of 100 steps from -50 mV to -10 mV for 100 ms at a rate of 1 Hz using samples in A. Higher detail of activation portion of trace is shown in inset. Dashed lines indicate the published N and C models. The boxplot below compares runtime of the simulations to generate the above traces for each model.

S3.4 I_{Kur}



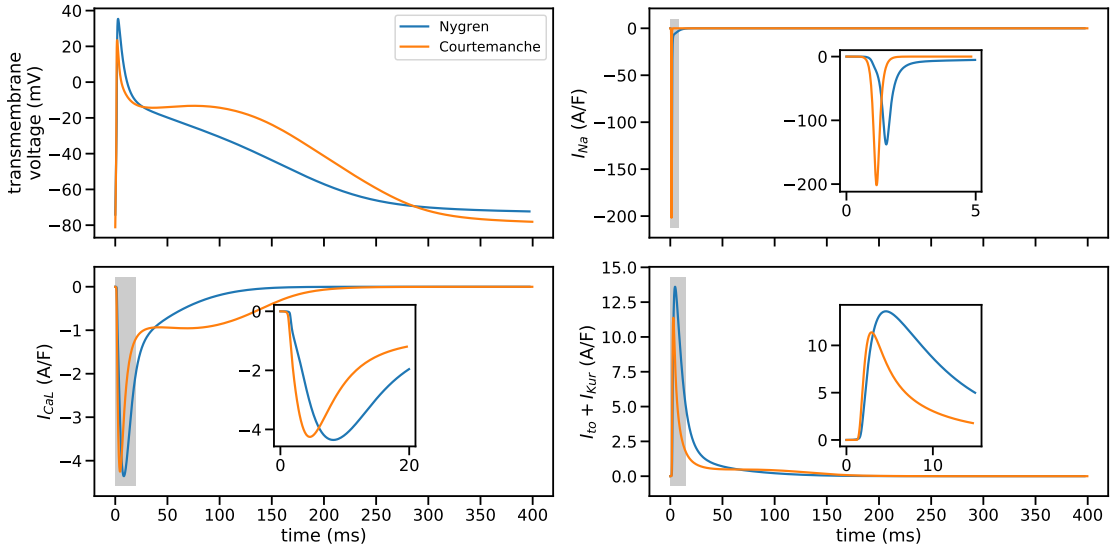
Supplementary Figure 10: **A** Results of calibrating each I_{Kur} model to the unified dataset. Model output is plotted as median with shading representing 89% HDPI generated from 100 samples from parameter posterior distributions. **B** Example traces from each model generated from the last step of a pulse train of 100 steps from -50 mV to -10 mV for 1000 ms at a rate of 0.1 Hz using samples from A. Dashed lines indicate the original N and C models. Higher detail of activation portion of trace is shown in inset plot. Boxplot compares runtime of simulations to generate the traces above for each model. **C** Steady-state and time constant functions for each gate generated from samples in A displayed as median lines with shading showing 89% HDPI. Dashed lines indicate original N and C models. **D** Number of gating parameters (top-left). Dark and light shading correspond to activation gate and inactivation gate parameters respectively. Goodness of fit assessed by converged residuals from ABC (top-right). RSD of parameter posteriors (bottom). Mann-Whitney U-test used to test significance.

S3.5 Goodness-of-fit residuals



Supplementary Figure 11: Min-max normalised residuals by experiment and model. Experiment ID follows order of appearance in main figure for that channel.

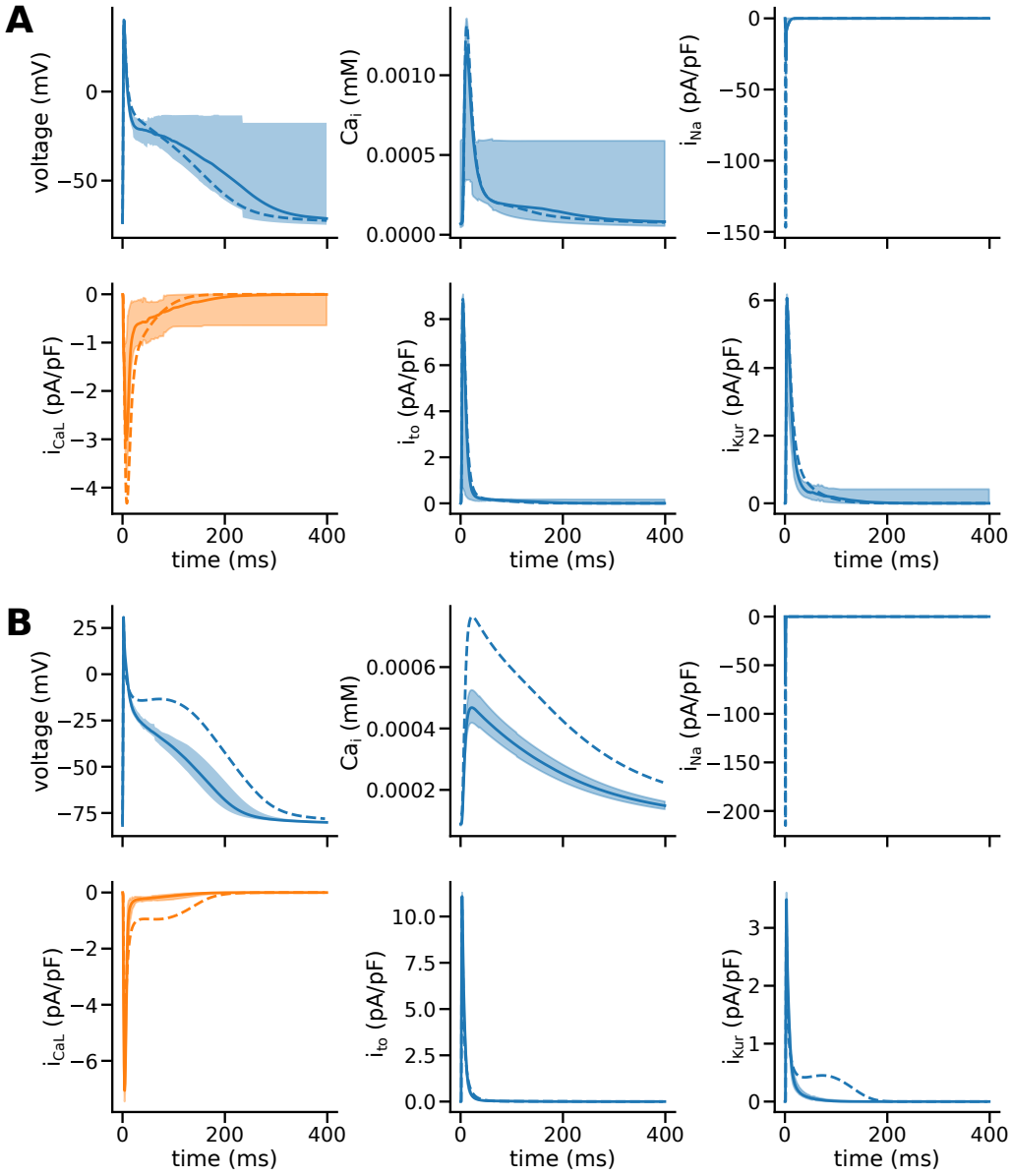
S3.6 Action potential response



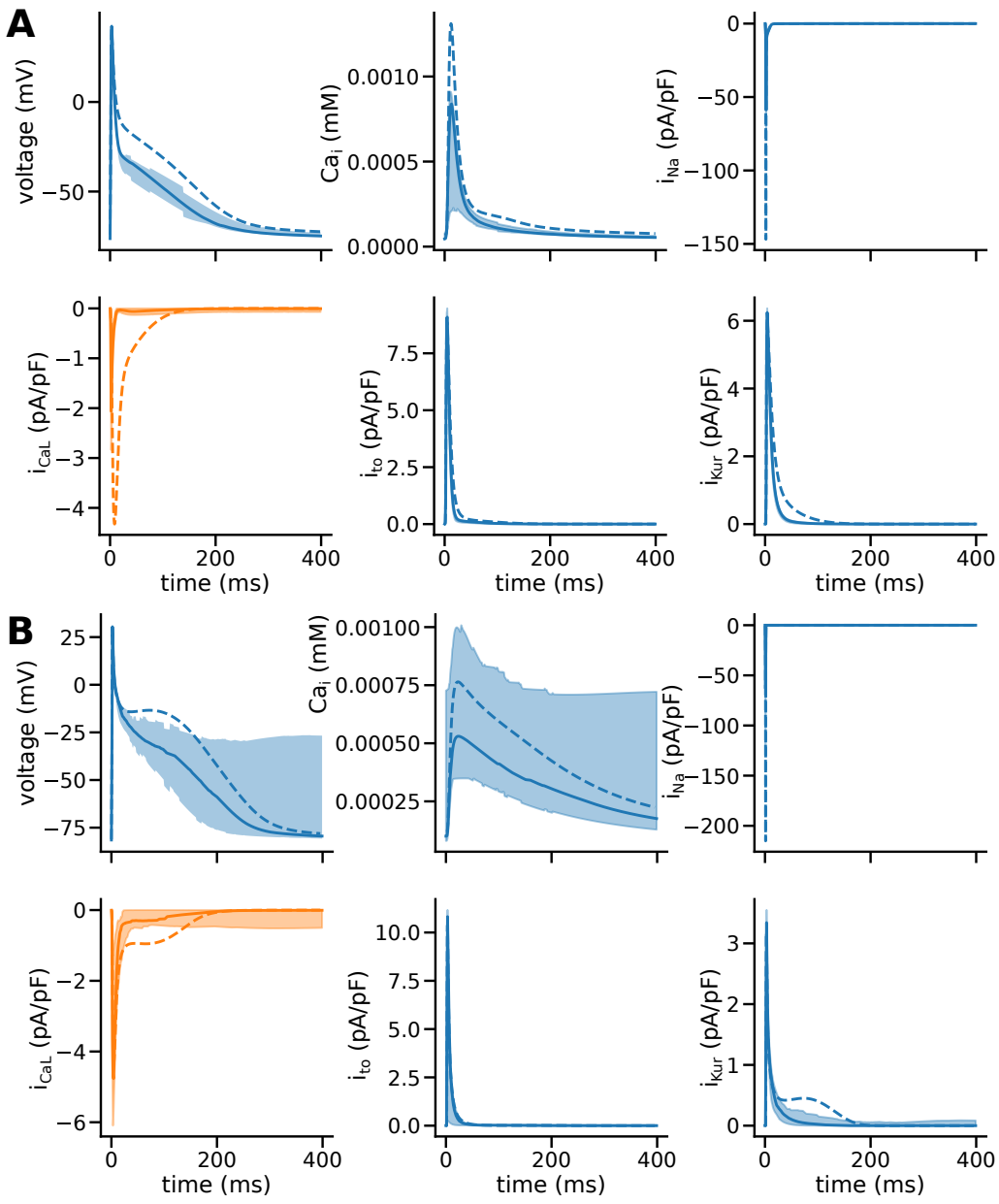
Supplementary Figure 12: Comparison of action potential morphology and major ion currents underlying the action potential in published N and C models of the human atrial cardiomyocyte. Inset graphs show more detail of the shaded time portion in the main graphs. Action potentials were stimulated by 100s of pacing at a basic cycle length of 1 s using a stimulus current of 40 pA/pF for 1 ms. The plot shows the final pulse from the pulse train protocol.

Model	Measure (units)	Published	I_{CaL} (89% HDPI)	I_{to} (89% HDPI)	I_{Kur} (89% HDPI)
N	RP (mV)	-74.1	-73.7 (-76.3, -17.5)	-72.7 (-72.7, -72.5)	-62.2 (-63.0, -61.4)
	AMP (mV)	114.3	113.4 (39.0, 115.8)	113.4 (113.1, 113.6)	95.0 (94.2, 95.8)
	APD90 (ms)	223.2	217.5 (16, 295)	271 (266, 280)	298 (295, 302)
C	RP (mV)	-81.2	-81.7 (-81.8, -81.6)	-81.3 (-81.4, -81.2)	-81.6 (-81.8, -80.9)
	AMP (mV)	110.9	112.5 (112.3, 112.9)	109.4 (107.5, 110.9)	111.2 (109.8, 111.8)
	APD90 (ms)	288.5	211 (189, 246)	257 (247, 266)	237.5 (190, 304)
N+S	RP (mV)	-74.1	-76.3 (-76.7, -70.3)	-73.2 (-73.2, -73.1)	-62.2 (-66.1, -58.0)
	AMP (mV)	114.3	118.6 (106.1, 120.3)	110.8 (110.6, 111.0)	93.9 (88.2, 98.8)
	APD90 (ms)	223.2	172.5 (131, 233)	248 (245, 249)	286 (283, 293)
C+S	RP (mV)	-81.2	-81.5 (-82.0, -27.1)	-81.2 (-81.2, -81.2)	-81.9 (-82.0, -81.8)
	AMP (mV)	110.9	111.7 (39.4, 112.9)	109.2 (109.1, 109.3)	107.6 (106.4, 108.9)
	APD90 (ms)	288.5	192 (35, ∞)	267 (264, 270)	179.5 (150, 206)

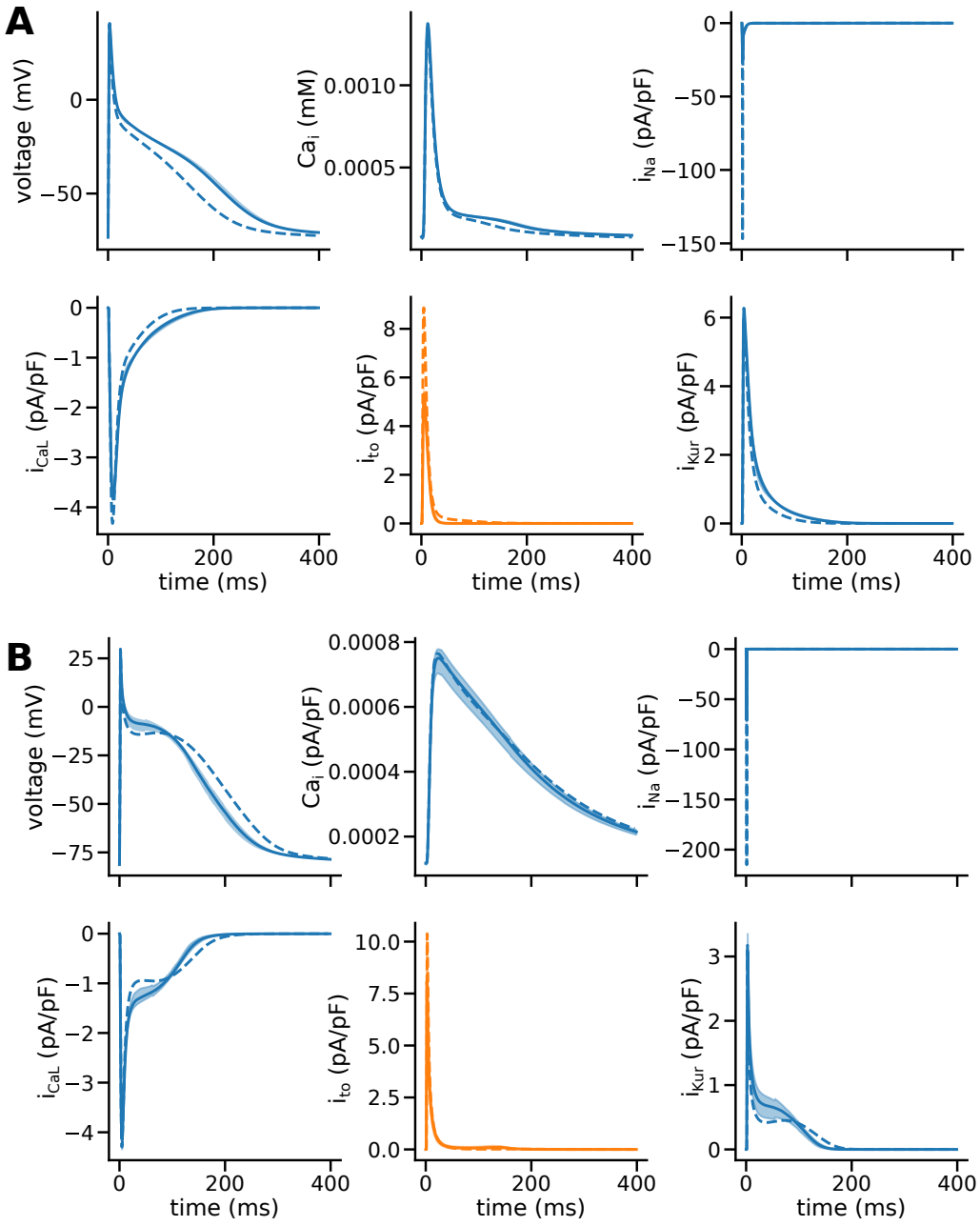
Supplementary Table 2: Effect on full AP of using parameter posterior distributions to calibrate channel models. Measurements taken are resting potential (RP), action potential amplitude (AMP) and action potential duration to 90% repolarisation (APD90). N: Nygren model, C: Courtemanche model, +S: represents the indicated channel was replaced with the standardised form in the full AP model.



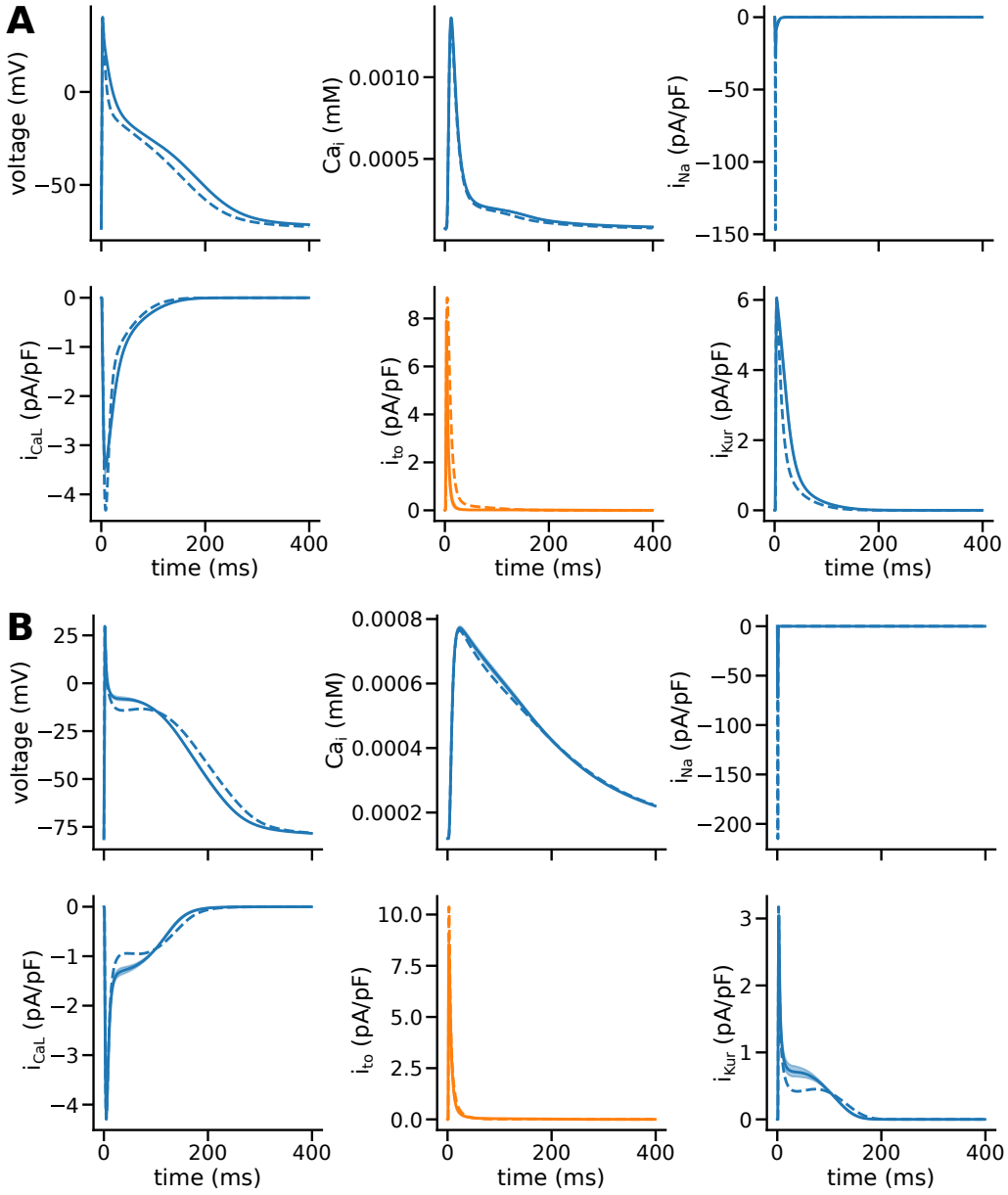
Supplementary Figure 13: Action potential, major currents and intracellular calcium concentrations for A: N model and B: C model. Traces using published parameters are represented with dashed lines. Samples from the full cell model with I_{CaL} replaced by the unified recalibrated parameterisation are displayed as a median line with 89% high density posterior intervals. The orange plot highlights the channel that is recalibrated using the parameter posterior distribution from ABC. All other model parameters are unchanged from published values.



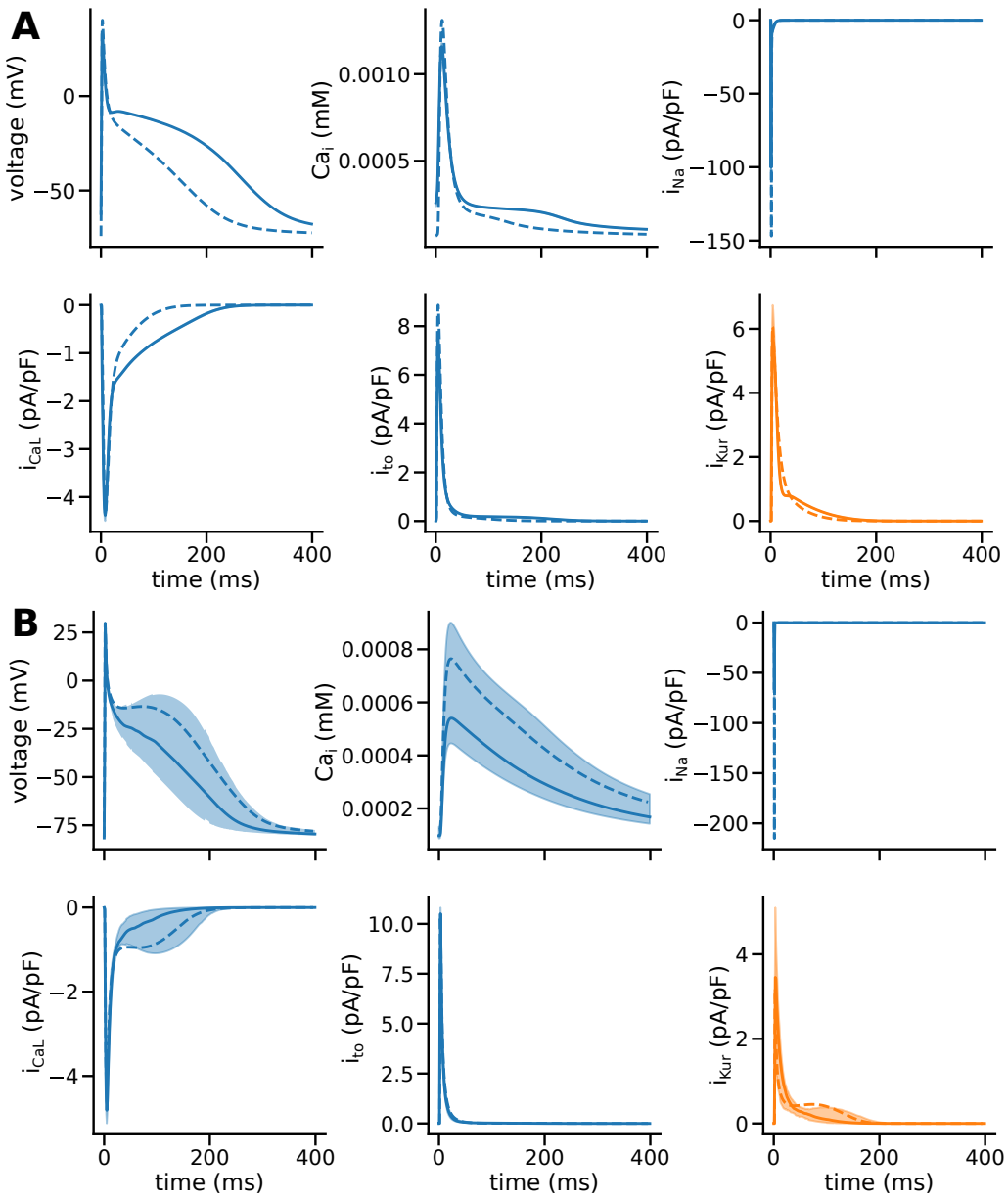
Supplementary Figure 14: Action potential, major currents and intracellular calcium concentrations for A: N model and B: C model, with the S form of I_{CaL} replacing the original form. Traces using published parameters are represented with dashed lines. Samples from the full cell model with I_{CaL} replaced by the unified recalibrated parameterisation are displayed as a median line with 89% high density posterior intervals. The orange plot highlights the channel that is replaced with the standardised model and using the parameter posterior distribution from ABC. All other model parameters are unchanged from published values.



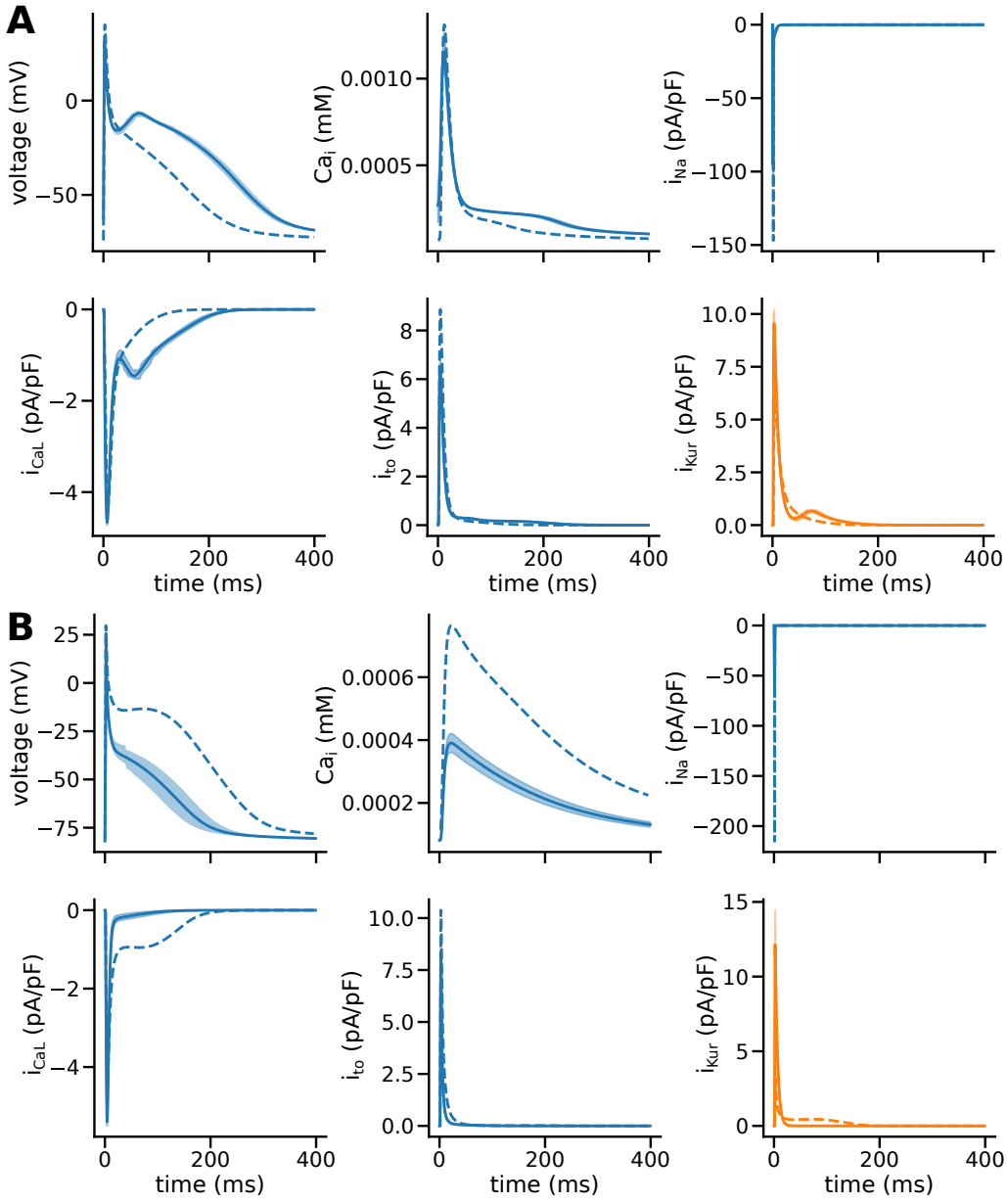
Supplementary Figure 15: Action potential, major currents and intracellular calcium concentrations for A: N model and B: C model. Traces using published parameters are represented with dashed lines. Samples from the full cell model with I_{to} replaced by the unified recalibrated parameterisation are displayed as a median line with 89% high density posterior intervals.. The orange plot highlights the channel that is recalibrated using the parameter posterior distribution from ABC. All other model parameters are unchanged from published values.



Supplementary Figure 16: Action potential, major currents and intracellular calcium concentrations for A: N model and B: C model, , with the S form of I_{to} replacing the original form. Traces using published parameters are represented with dashed lines. Samples from the full cell model with I_{to} replaced by the unified recalibrated parameterisation are displayed as a median line with 89% high density posterior intervals. The orange plot highlights the channel that is replaced with the standardised model and using the parameter posterior distribution from ABC. All other model parameters are unchanged from published values.



Supplementary Figure 17: Action potential, major currents and intracellular calcium concentrations for A: N model and B: C model. Traces using published parameters are represented with dashed lines. Samples from the full cell model with I_{Kur} replaced by the unified recalibrated parameterisation are displayed as a median line with 89% high density posterior intervals. The orange plot highlights the channel that is recalibrated using the parameter posterior distribution from ABC. All other model parameters are unchanged from published values.



Supplementary Figure 18: Action potential, major currents and intracellular calcium concentrations for A: N model and B: C model, , with the S form of I_{Kur} replacing the original form. Traces using published parameters are represented with dashed lines. Samples from the full cell model with I_{Kur} replaced by the unified recalibrated parameterisation are displayed as a median line with 89% high density posterior intervals. The orange plot highlights the channel that is replaced with the standardised model and using the parameter posterior distribution from ABC. All other model parameters are unchanged from published values.

S4 Model equations and numerical results

S4.1 I_{Na}

$$
\begin{aligned}
I_{\mathrm{Na}} &= P_{\mathrm{Na}} m^3 \left(\mathbf{s_1} h_1 + (1-\mathbf{s_1}) h_2\right) \left[\mathrm{Na}^+\right]_{\mathrm{c}} \mathrm{V} \frac{\mathrm{F}^2}{\mathrm{RT}} \frac{e^{(\mathrm{V}-\mathrm{E_{Na}})\mathrm{F}/\mathrm{RT}} - 1.0}{e^{\mathrm{VF}/\mathrm{RT}} - 1.0} \\
\frac{\mathrm{d}m}{\mathrm{dt}} &= \frac{\overline{m} - m}{\tau_m}, \qquad \frac{\mathrm{d}h_1}{\mathrm{dt}} = \frac{\overline{h} - h_1}{\tau_{h_1}}, \qquad \frac{\mathrm{d}h_2}{\mathrm{dt}} = \frac{\overline{h} - h_2}{\tau_{h_2}} \\
\overline{m} &= \frac{1.0}{1.0 + e^{-(\mathrm{V}+\mathbf{r_1})/\mathbf{r_2}}}, \qquad \tau_m = 1000(\mathbf{r_3} e^{-((\mathrm{V}+\mathbf{r_4})/\mathbf{r_5})^2} + \mathbf{r_6}) \\
\overline{h} &= \frac{1.0}{1.0 + e^{(\mathrm{V}+\mathbf{q_1})/\mathbf{q_2}}} \\
\tau_{h_1} &= 1000 \left(\frac{\mathbf{q_3}}{1.0 + e^{(\mathrm{V}+\mathbf{q_4})/\mathbf{q_5}}} + \mathbf{q_6} \right), \qquad \tau_{h_2} = 1000 \left(\frac{\mathbf{q_7}}{1.0 + e^{(\mathrm{V}+\mathbf{q_4})/\mathbf{q_5}}} + \mathbf{q_8} \right)
\end{aligned}
$$

Supplementary Table 3: Gating kinetics in Nygren model of I_{Na} channel current(see Table 6 in [1]). Time constants are multiplied by 1000 to convert from s to ms.

		Original				Unified		
Name	Published	Prior	Median	89% HDPI	$\log_{10}$RSD	Median	89% HDPI	$\log_{10}$RSD
r1	27.12	$\mathcal{U}$(0, 100)	52.25	(50.93, 53.52)	-1.795	42.83	(33.91, 55.13)	-0.7966
r2	8.21	$\mathcal{U}$(0, 20)	10.69	(9.769, 11.64)	-1.256	13.19	(7.761, 19.94)	-0.5127
r3*	4.2e-05	$\mathcal{U}$(-6, -3)	2.097e-05	(1.009e-06, 0.000325)	-0.749	1.371e-05	(1.002e-06, 0.0002247)	-0.7856
r4	25.57	$\mathcal{U}$(0, 100)	57.99	(22.82, 99.97)	-0.3404	56.79	(16.97, 99.79)	-0.293
r5	28.8	$\mathcal{U}$(0, 20)	9.979	(0.2856, 17.75)	-0.2282	8.932	(0.03437, 17.49)	-0.1981
r6*	2.4e-05	$\mathcal{U}$(-6, -3)	2.191e-05	(1.001e-06, 0.0005717)	-0.7021	9.662e-05	(5.195e-05, 0.0001536)	-1.43
q1	63.6	$\mathcal{U}$(0, 200)	95.57	(95.11, 96.11)	-2.465	93.94	(88.3, 99.55)	-1.4
q2	5.3	$\mathcal{U}$(0, 20)	6.5	(6.085, 6.841)	-1.432	8.182	(1.222, 13.13)	-0.3487
q3*	0.03	$\mathcal{U}$(-3, 0)	0.09214	(0.001002, 0.4502)	-0.1696	0.004096	(0.002543, 0.02547)	-0.7312
q4	35.1	$\mathcal{U}$(0, 100)	34.98	(0.1474, 147.7)	-0.02249	53.57	(48.79, 57.53)	-1.263
q5	3.2	$\mathcal{U}$(0, 20)	12.76	(4.548, 19.99)	-0.361	10.61	(7.184, 13.18)	-0.7463
q6*	0.0003	$\mathcal{U}$(-5, -2)	0.0002548	(1.002e-05, 0.004472)	-0.6137	0.0002403	(1.006e-05, 0.001556)	-0.7811
q7*	0.12	$\mathcal{U}$(-3, 0)	0.07443	(0.001005, 0.3999)	-0.1983	0.02022	(0.002551, 0.02706)	-0.6835
q8*	0.003	$\mathcal{U}$(-4, -1)	0.002224	(0.0001001, 0.04665)	-0.4589	0.0005268	(0.0001001, 0.00171)	-0.9219
s1	0.9	$\mathcal{U}$(0, 1)	0.5015	(0.08985, 0.9754)	-0.2317	0.4717	(0.1367, 0.8259)	-0.334

Supplementary Table 4: Summary of results for parameters of Nygren I_{Na} model using original and unified dataset. *Parameters were searched in $\log_{10}$ space based on the scale of their published values and are presented in linear space. The prior for these parameters is still in the original $\log_{10}$ space.

$$
\begin{aligned}
I_{\mathrm{Na}} &= g_{\mathrm{Na}} m^3 h j (\mathrm{V} - \mathrm{E_{Na}}) \\
\frac{\mathrm{d}\phi}{\mathrm{dt}} &= \frac{\phi_\infty - \phi}{\tau_\phi}, \qquad \text{for } \phi = m, h, j \\
\tau_\phi &= (\alpha_\phi + \beta_\phi)^{-1}, \qquad \phi_\infty = \alpha_\phi \tau_\phi, \qquad \text{for } \phi = m, h, j \\
\alpha_m &= \begin{cases} \mathbf{a_{m,2}} \frac{\mathrm{V} - \mathbf{a_{m,1}}}{1 - e^{-\mathbf{a_{m,3}}(\mathrm{V} - \mathbf{a_{m,1}})}} \\ \mathbf{a_{m,4}}, \text{ if } \mathrm{V} = \mathbf{a_{m,1}} \end{cases}, \qquad \beta_m = \mathbf{b_{m,1}} e^{-\mathrm{V}/\mathbf{b_{m,2}}} \\
\alpha_h &= \begin{cases} \mathbf{a_{h,1}} e^{(\mathrm{V} + \mathbf{a_{h,3}})/-\mathbf{a_{h,2}}} \\ a_{h,5}, \qquad \text{if } \mathrm{V} \geq \mathbf{c_{h,1}} \end{cases}, \qquad a_{h,5} = \mathbf{a_{h,1}} e^{(\mathbf{c_{h,1}} + \mathbf{a_{h,3}})/-\mathbf{a_{h,2}}} \\
\beta_h &= \begin{cases} \mathbf{b_{h,4}} e^{\mathbf{b_{h,5}}\mathrm{V}} + \mathbf{b_{h,6}} e^{\mathbf{b_{h,7}}\mathrm{V}} \\ \left(b_{h,1}\left[1.0 + e^{(V + \mathbf{b_{h,2}})/-\mathbf{b_{h,3}}}\right]\right)^{-1}, \quad \text{if } V \geq \mathbf{c_{h,1}} \end{cases} \\
b_{h,1} &= \left(\mathbf{b_{h,4}} e^{\mathbf{b_{h,5}}\mathbf{c_{h,1}}} + \mathbf{b_{h,6}} e^{\mathbf{b_{h,7}}\mathbf{c_{h,1}}}\right)^{-1} \left(1.0 + e^{(\mathbf{c_{h,1}} + \mathbf{b_{h,2}})/-\mathbf{b_{h,3}}}\right)^{-1} \\
\alpha_j &= \begin{cases} \left[-\mathbf{a_{j,1}} e^{\mathbf{a_{j,2}}\mathrm{V}} - \mathbf{a_{j,3}} e^{-\mathbf{a_{j,4}}\mathrm{V}}\right] \frac{\mathrm{V} + a_{j,5}}{1.0 + e^{\mathbf{a_{j,6}}(\mathrm{V} + \mathbf{a_{j,7}})}} \\ 0, \quad \text{if } V \geq \mathbf{c_{j,1}} \end{cases}, \qquad a_{j,5} = -\mathbf{c_{j,1}} \\
\beta_j &= \begin{cases} \mathbf{b_{j,5}} \frac{e^{-\mathbf{b_{j,6}}\mathrm{V}}}{1 + e^{-\mathbf{b_{j,7}}(\mathrm{V} + \mathbf{b_{j,8}})}} \\ b_{j,1} \frac{e^{-b_{j,2}\mathrm{V}}}{1 + e^{-\mathbf{b_{j,3}}(\mathrm{V} + \mathbf{b_{j,4}})}}, \quad \text{if } V \geq \mathbf{c_{j,1}} \end{cases}, \\
b_{j,1} &= \mathbf{b_{j,5}} \frac{e^{-\mathbf{b_{j,6}}\mathbf{c_{j,1}}}}{1 + e^{-\mathbf{b_{j,7}}(\mathbf{c_{j,1}} + \mathbf{b_{j,8}})}} \left[\frac{e^{-b2_j \mathbf{c_{j,1}}}}{(1 + e^{-\mathbf{b_{j,3}}(\mathbf{c_{j,1}} + \mathbf{b_{j,4}})}}\right]^{-1}, \qquad b_{j,2} = 0.0
\end{aligned}
$$

Supplementary Table 5: Gating kinetics in Courtemanche model of I_{Na} channel current (see Appendix in [2]). Values of $a_{h,5}$, $b_{h,1}$, $a_{j,5}$ and $b_{j,1}$ are set to enforce continuity in piecewise functions. $b_{j,2}$ is set to zero to reduce dimensionality of the calibration problem as the published parameter was effectively zero (2.535×10^{-7}).

Original/Unified					
Name	Published	Prior	Median	89% HDPI	$\log_{10}$RSD
$a1_m$	-47.13	$\mathcal{U}(-100, 0)$	-75.97	(-79.77, -73.65)	-1.586
$a2_m$	0.32	$\mathcal{U}(0, 1)$	0.2639	(0.2476, 0.2741)	-1.476
$a3_m$	0.1	$\mathcal{U}(0, 1)$	0.3355	(0.1947, 0.7643)	-0.2765
$a4_m$	3.2	$\mathcal{U}(0, 10)$	4.895	(1.699, 9.998)	-0.2421
$b1_m$	0.08	$\mathcal{U}(0, 10)$	1.263	(1.225, 1.322)	-1.64
$b2_m$	11.0	$\mathcal{U}(0, 100)$	23.21	(22.48, 23.74)	-1.774
$a1_h^*$	0.135	$\mathcal{U}(-2, 1)$	0.3845	(0.01157, 3.35)	0.269
$a2_h$	6.8	$\mathcal{U}(0, 50)$	15.48	(14.49, 15.99)	-1.465
$a3_h$	80.0	$\mathcal{U}(0, 200)$	122.2	(67.51, 155.4)	-0.6085
$b2_h$	10.66	$\mathcal{U}(0, 100)$	18.35	(5.525, 31.86)	-0.3218
$b3_h$	11.1	$\mathcal{U}(0, 50)$	16.73	(12.42, 21.47)	-0.7582
$b4_h^*$	3.56	$\mathcal{U}(-1, 2)$	15.11	(14.51, 15.79)	-1.999
$b5_h^*$	0.079	$\mathcal{U}(-3, 0)$	0.05808	(0.05716, 0.05887)	-2.492
$b6_h^*$	310000.0	$\mathcal{U}(3, 6)$	21500.0	(1002.0, 321300.0)	-0.6777
$b7_h^*$	0.35	$\mathcal{U}(-2, 1)$	1.327	(0.2776, 6.324)	0.4741
$c1_h$	-40.0	$\mathcal{U}(-100, 0)$	-37.27	(-45.94, -32.91)	-0.8902
$a1_j^*$	127100.0	$\mathcal{U}(3, 7)$	123700.0	(1180.0, 4778000.0)	-0.6361
$a2_j^*$	0.2444	$\mathcal{U}(-2, 2)$	5.144	(0.1528, 50.75)	0.02476
$a3_j^*$	3.474e-05	$\mathcal{U}(-5, -1)$	0.0003798	(1.015e-05, 0.001191)	-0.7783
$a4_j^*$	0.04391	$\mathcal{U}(-4, 0)$	0.003784	(0.0001, 0.02896)	-0.5131
$a6_j$	0.311	$\mathcal{U}(0, 1)$	0.4461	(0.01244, 0.8846)	-0.2087
$a7_j$	79.23	$\mathcal{U}(0, 100)$	41.53	(4.671, 91.36)	-0.1966
$b3_j$	0.1	$\mathcal{U}(0, 1)$	0.4481	(0.001746, 0.8611)	-0.1977
$b4_j$	32.0	$\mathcal{U}(0, 100)$	67.64	(21.51, 99.97)	-0.3641
$b5_j$	0.1212	$\mathcal{U}(0, 1)$	0.3552	(0.04405, 0.7968)	-0.1691
$b6_j^*$	0.01052	$\mathcal{U}(-4, 0)$	0.001531	(0.0001004, 0.01829)	-0.5618
$b7_j$	0.1378	$\mathcal{U}(0, 1)$	0.2679	(0.0008117, 0.7773)	-0.09422
$b8_j$	40.14	$\mathcal{U}(0, 100)$	72.38	(31.39, 99.94)	-0.4359
$c1_j$	-40.0	$\mathcal{U}(-100, 0)$	-33.07	(-74.3, -0.5147)	-0.179

Supplementary Table 6: Summary of results for parameters of Courtemanche I_{Na} model using original/unified (equivalent) dataset. *Parameters were searched in $\log_{10}$ space based on the scale of their published values and are presented in linear space. The prior for these parameters is still in the original $\log_{10}$ space.

Unified				
Name	Prior	Median	89% HDPI	$\log_{10}$RSD
p_1^*	$\mathcal{U}$(1, 5)	5134.0	(1620.0, 9786.0)	-1.241
p_2	$\mathcal{U}$(1e-7, 0.2)	0.126	(0.1048, 0.1524)	-0.9488
p_3^*	$\mathcal{U}$(-3, 1)	3.374	(0.5586, 6.144)	-0.2008
p_4	$\mathcal{U}$(1e-7, 0.4)	0.0234	(0.002225, 0.04426)	-0.2237
p_5^*	$\mathcal{U}$(-1, 3)	6.091	(5.572, 6.662)	-1.495
p_6	$\mathcal{U}$(1e-7, 0.2)	0.0441	(0.04209, 0.04601)	-1.523
p_7^*	$\mathcal{U}$(-4, 0)	0.005353	(0.004147, 0.006667)	-1.496
p_8	$\mathcal{U}$(1e-7, 0.2)	0.04053	(0.03871, 0.04302)	-1.44
A^*	$\mathcal{U}$(0, 1)	4.195	(4.049, 4.314)	-1.869

Supplementary Table 7: Summary of results for parameters of standardised I_{Na} model using unified dataset. *Parameters were searched in $\log_{10}$ space and are presented in linear space. The prior for these parameters is still in the original $\log_{10}$ space.

S4.2 I_{CaL}

$$
\begin{aligned}
I_{\mathrm{CaL}} &= \bar{g}_{\mathrm{Ca,L}} d_{\mathrm{L}} \left[f_{\mathrm{Ca}} f_{\mathrm{L}_1} + (1 - f_{\mathrm{Ca}}) f_{\mathrm{L}_2} \right] (\mathrm{V} - \mathrm{E}_{\mathrm{Ca,app}}) \\
\frac{\mathrm{d}d_{\mathrm{L}}}{\mathrm{dt}} &= \frac{\overline{d_{\mathrm{L}}} - d_{\mathrm{L}}}{\tau_{d_{\mathrm{L}}}}, \qquad \frac{\mathrm{d}f_{\mathrm{L}_1}}{\mathrm{dt}} = \frac{\overline{f_{\mathrm{L}}} - f_{\mathrm{L}_1}}{\tau_{f_{\mathrm{L}_1}}}, \qquad \frac{\mathrm{d}f_{\mathrm{L}_2}}{\mathrm{dt}} = \frac{\overline{f_{\mathrm{L}}} - f_{\mathrm{L}_2}}{\tau_{f_{\mathrm{L}_2}}} \\
\overline{d_{\mathrm{L}}} &= \frac{1.0}{1.0 + e^{(\mathrm{V}+\mathbf{p_1})/-\mathbf{p_2}}}, \qquad \tau_{d_{\mathrm{L}}} = 1000 \left(\mathbf{p_3} e^{-((\mathrm{V}+\mathbf{p_4})/\mathbf{p_5})^2} + \mathbf{p_6} \right) \\
\overline{f_{\mathrm{L}}} &= \frac{1.0}{1.0 + e^{(\mathrm{V}+\mathbf{q_1})/\mathbf{q_2}}} \\
\tau_{f_{\mathrm{L}_1}} &= 1000 \left(\mathbf{q_3} e^{-((\mathrm{V}+\mathbf{q_4})/\mathbf{q_5})^2} + \mathbf{q_6} \right), \qquad \tau_{f_{\mathrm{L}_2}} = 1000 \left(\mathbf{r_1} e^{-((\mathrm{V}+\mathbf{r_2})/\mathbf{r_3})^2} + \mathbf{r_4} \right)
\end{aligned}
$$

Supplementary Table 8: Gating kinetics in Nygren model of I_{CaL} channel current (see Table 7 in [1]). Time constants are multiplied by 1000 to convert from s to ms.

		Original				Unified		
Name	Published	Prior	Median	89% HDPI	$\log_{10}$RSD	Median	89% HDPI	$\log_{10}$RSD
p1	9.0	$\mathcal{U}$(-100, 100)	2.684	(2.529, 2.906)	-1.29	9.317	(5.103, 10.51)	-0.5683
p2	5.8	$\mathcal{U}$(0, 50)	5.055	(5.022, 5.083)	-2.416	7.378	(6.679, 8.916)	-0.9407
p3*	0.0027	$\mathcal{U}$(-7, 3)	0.1048	(0.096, 0.1063)	-1.869	0.001129	(1e-07, 0.02533)	-0.2353
p4	35.0	$\mathcal{U}$(-100, 100)	-11.51	(-11.6, -11.36)	-2.151	-39.18	(-99.98, 74.02)	0.4508
p5	30.0	$\mathcal{U}$(0, 50)	18.58	(18.39, 18.86)	-2.078	28.21	(6.568, 49.05)	-0.2817
p6*	0.002	$\mathcal{U}$(-7, 3)	0.00996	(0.009237, 0.0108)	-1.919	0.0009303	(1.027e-07, 0.0009643)	-0.5757
q1	27.4	$\mathcal{U}$(0, 100)	32.02	(21.21, 47.51)	-0.5415	32.02	(21.21, 47.51)	-0.5415
q2	7.1	$\mathcal{U}$(0, 50)	8.06	(1.553, 18.14)	-0.2068	8.06	(1.553, 18.14)	-0.2068
q3*	0.161	$\mathcal{U}$(-7, 3)	0.04208	(1.103e-07, 0.7733)	-0.002009	0.04208	(1.103e-07, 0.7733)	-0.002009
q4	40.0	$\mathcal{U}$(0, 100)	59.81	(29.52, 99.4)	-0.3934	59.81	(29.52, 99.4)	-0.3934
q5	14.4	$\mathcal{U}$(0, 50)	25.73	(2.594, 43.97)	-0.2737	25.73	(2.594, 43.97)	-0.2737
q6*	0.01	$\mathcal{U}$(-7, 3)	0.007372	(0.002444, 0.05932)	-0.5916	0.007372	(0.002444, 0.05932)	-0.5916
r1*	1.332	$\mathcal{U}$(-7, 3)	0.05255	(1.14e-07, 2.713)	0.05333	0.05255	(1.14e-07, 2.713)	0.05333
r2	40.0	$\mathcal{U}$(0, 100)	45.95	(13.92, 96.56)	-0.2224	45.95	(13.92, 96.56)	-0.2224
r3	14.2	$\mathcal{U}$(0, 100)	46.89	(0.5929, 88.34)	-0.1519	46.89	(0.5929, 88.34)	-0.1519
r4*	0.0626	$\mathcal{U}$(-7, 3)	0.01455	(1.051e-07, 0.05889)	-0.2101	0.01455	(1.051e-07, 0.05889)	-0.2101

Supplementary Table 9: Summary of results for parameters of Nygren I_{CaL} model. Only activation parameters (p) recalibrated to unified dataset. *Parameters were searched in $\log_{10}$ space based on the scale of their published values and are presented in linear space. The prior for these parameters is still in the original $\log_{10}$ space.

$$
\begin{aligned}
I_{\mathrm{CaL}} &= g_{\mathrm{Ca,L}} d f f_{\mathrm{Ca}} (\mathrm{V} - \mathrm{E}_{\mathrm{Ca,app}}) \\
\frac{\mathrm{d}d}{\mathrm{dt}} &= \frac{\overline{d} - d}{\tau_d}, \qquad \frac{\mathrm{d}f}{\mathrm{dt}} = \frac{\overline{f} - f}{\tau_f} \\
\overline{d} &= \frac{1.0}{1.0 + e^{(\mathrm{V}+\mathbf{p_4})/-\mathbf{p_5}}}, \qquad \tau_d = \frac{1 - e^{(\mathrm{V}+\mathbf{p_1})/-\mathbf{p_2}}}{\mathbf{p_3}(\mathrm{V} + \mathbf{p_1})\left[1 + e^{(\mathrm{V}+\mathbf{p_1})/-\mathbf{p_2}}\right]} \\
\overline{f} &= \frac{1.0}{1.0 + e^{(\mathrm{V}+\mathbf{q_6})/\mathbf{q_7}}}, \qquad \tau_f = \mathbf{q_1}\left[\mathbf{q_2} e^{-\mathbf{q_3}^2 (\mathrm{V}+\mathbf{q_4})^2} + \mathbf{q_5}\right]^{-1}
\end{aligned}
$$

Supplementary Table 10: Gating kinetics in Courtemanche model of I_{CaL} channel current (see Appendix in [2]).

		Original			Unified			
Name	Published	Prior	Median	89% HDPI	$\log_{10}$RSD	Median	89% HDPI	$\log_{10}$RSD
p1	10.0	$\mathcal{U}$(-100, 100)	-63.91	(-90.59, -30.08)	-0.5153	-38.24	(-99.15, 54.23)	0.2831
p2	6.24	$\mathcal{U}$(0, 50)	9.655	(1.853, 18.57)	-0.2793	19.17	(0.1832, 43.09)	-0.1334
p3*	0.035	$\mathcal{U}$(-7, 3)	2.072e-07	(1.559e-07, 0.0001709)	-0.6749	0.02479	(0.01392, 0.0721)	-0.7863
p4	10.0	$\mathcal{U}$(-100, 100)	19.07	(6.624, 20.71)	-0.5022	10.44	(10.05, 10.71)	-1.66
p5	8.0	$\mathcal{U}$(0, 50)	6.078	(5.647, 7.053)	-1.029	7.447	(7.267, 7.638)	-1.754
q1*	9.0	$\mathcal{U}$(0, 3)	57.97	(1.072, 435.5)	-0.372	5.315	(1.004, 19.81)	-0.2447
q2*	0.0197	$\mathcal{U}$(-2, 3)	0.2487	(0.01006, 3.008)	0.2592	1.825	(0.1754, 6.422)	0.3113
q3*	0.0337	$\mathcal{U}$(-4, 0)	0.01259	(0.0001002, 0.1925)	-0.3061	0.1147	(0.08051, 0.1534)	-1.006
q4	10.0	$\mathcal{U}$(-100, 100)	-11.13	(-71.3, 88.69)	0.8784	1.305	(-1.347, 4.125)	0.07887
q5*	0.02	$\mathcal{U}$(-4, 0)	0.02488	(0.0001023, 0.4122)	-0.1906	0.1955	(0.03626, 0.6931)	-0.2331
q6	28.0	$\mathcal{U}$(-100, 100)	27.82	(25.28, 30.52)	-1.177	33.32	(25.89, 40.27)	-0.8614
q7	6.9	$\mathcal{U}$(0, 50)	6.879	(5.583, 8.993)	-0.8052	10.95	(7.257, 13.98)	-0.704

Supplementary Table 11: Summary of results of parameters of Courtemanche I_{CaL} model. *Parameters were searched in $\log_{10}$ space based on the scale of their published values and are presented in linear space. The prior for these parameters is still in the original $\log_{10}$ space.

Unified				
Name	Prior	Median	89% HDPI	$\log_{10}$RSD
p_1^*	$\mathcal{U}$(-7, 3)	0.5513	(1.02e-07, 1.073)	0.1053
p_2	$\mathcal{U}$(1e-7, 0.4)	0.01878	(1.245e-05, 0.05856)	-0.07143
p_3^*	$\mathcal{U}$(-7, 3)	0.375	(0.0056, 1.575)	0.07778
p_4	$\mathcal{U}$(1e-7, 0.4)	0.09998	(0.02278, 0.2473)	-0.1811
p_5^*	$\mathcal{U}$(-7, 3)	0.06489	(0.04241, 0.2347)	-0.6597
p_6	$\mathcal{U}$(1e-7, 0.4)	0.04437	(0.03053, 0.06118)	-0.6387
p_7^*	$\mathcal{U}$(-7, 3)	0.02056	(0.01379, 0.02842)	-1.205
p_8	$\mathcal{U}$(1e-7, 0.4)	0.02449	(0.01303, 0.03353)	-0.5575
A^*	$\mathcal{U}$(0, 3)	4.497	(3.235, 13.56)	-0.5354

Supplementary Table 12: Summary of results of parameters of standardised I_{CaL} model using unified dataset. *Parameters were searched in $\log_{10}$ space and are presented in linear space. The prior for these parameters is still in the original $\log_{10}$ space.

S4.3 I_{to}

$$
\begin{aligned}
I_{\text{to}} &= \bar{g}_{\text{t}} r s \left(\text{V} - \text{E}_{\text{K}}\right) \\
\frac{\text{d}r}{\text{dt}} &= \frac{\overline{r} - r}{\tau_r}, \qquad \frac{\text{d}s}{\text{dt}} = \frac{\overline{s} - s}{\tau_s} \\
\overline{r} &= \frac{1.0}{1.0 + e^{(\text{V} - \mathbf{p_1})/-\mathbf{p_2}}}, \qquad \tau_r = 1000 \left(\mathbf{p_3} e^{-(\text{V}/\mathbf{p_4})^2} + \mathbf{p_5}\right) \\
\overline{s} &= \frac{1.0}{1.0 + e^{(\text{V} + \mathbf{q_1})/\mathbf{q_2}}}, \qquad \tau_s = 1000 \left(\mathbf{q_3} e^{-((\text{V} + \mathbf{q_4})/\mathbf{q_5})^2} + \mathbf{q_6}\right)
\end{aligned}
$$

Supplementary Table 13: Gating kinetics in Nygren model of I_{to} channel current (see Table 8 in [1]). Time constants are multiplied by 1000 to convert from s to ms.

		Original				Unified		
Name	Published	Prior	Median	89% HDPI	$\log_{10}$RSD	Median	89% HDPI	$\log_{10}$RSD
p1	1.0	$\mathcal{U}$(-100, 100)	3.25	(0.3302, 6.375)	-0.234	-0.577	(-7.205, 2.269)	0.4008
p2	11.0	$\mathcal{U}$(1e-7, 50)	10.32	(7.678, 12.61)	-0.8453	2.197	(1.381, 2.753)	-0.6039
p3*	0.0035	$\mathcal{U}$(-7, 0)	4.613e-06	(1.013e-07, 0.0001495)	-0.6929	0.008113	(0.007376, 0.008801)	-1.931
p4	30.0	$\mathcal{U}$(1e-7, 50)	22.81	(0.2115, 43.89)	-0.2055	43.54	(40.81, 46.05)	-1.426
p5*	0.0015	$\mathcal{U}$(-7, 0)	0.002083	(1.005e-07, 0.004469)	-0.4898	0.001244	(0.00109, 0.00137)	-1.973
q1	40.5	$\mathcal{U}$(-100, 100)	54.85	(21.94, 90.84)	-0.4189	28.97	(27.85, 30.79)	-1.473
q2	11.5	$\mathcal{U}$(1e-7, 50)	15.86	(5.989, 22.65)	-0.4416	1.161	(0.3452, 1.969)	-0.3639
q3*	0.4812	$\mathcal{U}$(-5, 1)	0.3981	(0.3359, 0.5484)	-0.6558	0.09093	(0.08613, 0.09628)	-1.829
q4	52.45	$\mathcal{U}$(-100, 100)	57.94	(49.6, 63.12)	-1.104	38.16	(37.65, 38.63)	-2.083
q5	14.97	$\mathcal{U}$(1e-7, 50)	12.1	(9.079, 16.57)	-0.7154	16.87	(16.17, 17.58)	-1.577
q6*	0.01414	$\mathcal{U}$(-7, 0)	0.01171	(0.009782, 0.01371)	-1.577	0.008563	(0.008114, 0.008981)	-2.178

Supplementary Table 14: Summary of results for parameters of Nygren I_{to} model. *Parameters were searched in $\log_{10}$ space based on the scale of their published values and are presented in linear space. The prior for these parameters is still in the original $\log_{10}$ space.

$$
\begin{aligned}
I_{\text{to}} &= g_{\text{to}} o_{\text{a}}^3 o_{\text{i}} \left(\text{V} - \text{E}_{\text{K}}\right) \\
\frac{\text{d}\phi}{\text{dt}} &= \frac{\phi_\infty - \phi}{\tau_\phi}, \qquad \text{for } \phi = o_{\text{a}}, o_{\text{i}} \\
\tau_\phi &= \left(\alpha_\phi + \beta_\phi\right)^{-1}, \qquad \text{for } \phi = o_{\text{a}}, o_{\text{i}} \\
o_{\text{a}(\infty)} &= \frac{1.0}{1.0 + e^{(\text{V}+\mathbf{p_1})/-\mathbf{p_2}}}, \qquad \alpha_{o(\text{a})} = \frac{\mathbf{p_3}}{e^{(\text{V}+\mathbf{p_4})/-\mathbf{p_5}} + e^{(\text{V}+\mathbf{p_6})/-\mathbf{p_7}}}, \qquad \beta_{o(\text{a})} = \frac{\mathbf{p_3}}{\mathbf{p_8} + e^{(\text{V}+\mathbf{p_9})/\mathbf{p_{10}}}} \\
o_{\text{i}(\infty)} &= \frac{1.0}{1.0 + e^{(\text{V}+\mathbf{q_1})/\mathbf{q_2}}}, \qquad \alpha_{o(\text{i})} = \frac{1.0}{\mathbf{q_3} + e^{(\text{V}+\mathbf{q_4})/\mathbf{q_5}}}, \qquad \beta_{o(\text{i})} = \frac{1.0}{\mathbf{q_6} + e^{(\text{V}+\mathbf{q_7})/-\mathbf{q_8}}}
\end{aligned}
$$

Supplementary Table 15: Gating kinetics in Courtemanche model of I_{to} channel current (see Appendix in [2]).

		Original/Unified			
Name	Published	Prior	Median	89% HDPI	$\log_{10}$RSD
p1	20.47	$\mathcal{U}$(-100, 100)	16.34	(7.558, 24.01)	-0.5041
p2	17.54	$\mathcal{U}$(1e-7, 50)	19.03	(14.78, 23.36)	-0.8263
p3*	0.65	$\mathcal{U}$(-3, 2)	0.06738	(0.002023, 0.259)	-0.3748
p4	10.0	$\mathcal{U}$(-100, 100)	28.32	(-0.545, 81.34)	-0.1259
p5	8.5	$\mathcal{U}$(1e-7, 50)	12.98	(0.01876, 41.94)	-0.09246
p6	-30.0	$\mathcal{U}$(-100, 100)	23.19	(4.345, 94.19)	-0.07312
p7	59.0	$\mathcal{U}$(1e-7, 100)	10.41	(0.008675, 37.07)	-0.05074
p8*	2.5	$\mathcal{U}$(-3, 2)	0.1598	(0.001051, 2.304)	0.04982
p9	82.0	$\mathcal{U}$(-100, 100)	62.09	(-8.713, 99.55)	-0.08063
p10	17.0	$\mathcal{U}$(1e-7, 50)	41.35	(21.91, 49.99)	-0.5362
q1	43.1	$\mathcal{U}$(-100, 100)	33.51	(30.65, 35.14)	-1.353
q2	5.3	$\mathcal{U}$(1e-7, 50)	6.981	(5.946, 8.025)	-0.8174
q3*	18.53	$\mathcal{U}$(-1, 4)	3.668	(0.1006, 14.48)	0.1733
q4	113.7	$\mathcal{U}$(0, 200)	125.8	(114.5, 135.2)	-1.178
q5	10.95	$\mathcal{U}$(1e-7, 50)	15.42	(13.43, 17.26)	-0.9771
q6*	35.56	$\mathcal{U}$(-1, 4)	37.67	(36.17, 41.82)	-1.898
q7	1.26	$\mathcal{U}$(-100, 100)	31.78	(27.76, 36.86)	-0.7325
q8	7.44	$\mathcal{U}$(1e-7, 50)	0.6272	(0.003919, 1.28)	0.1188

Supplementary Table 16: Summary of results for parameters of Courtemanche I_{to} model. Original and unified datasets are equivalent. *Parameters were searched in $\log_{10}$ space based on the scale of their published values and are presented in linear space. The prior for these parameters is still in the original $\log_{10}$ space.

Unified				
Name	Prior	Median	89% HDPI	$\log_{10}$RSD
p_1^*	$\mathcal{U}$(-7, 3)	0.00556	(0.005179, 0.006032)	-1.904
p_2	$\mathcal{U}$(1e-7, 0.4)	0.07096	(0.06763, 0.07326)	-1.586
p_3^*	$\mathcal{U}$(-7, 3)	0.1906	(0.1817, 0.1991)	-1.774
p_4	$\mathcal{U}$(1e-7, 0.4)	0.02528	(0.02459, 0.0261)	-1.724
p_5^*	$\mathcal{U}$(-7, 3)	0.1066	(0.1019, 0.1129)	-1.83
p_6	$\mathcal{U}$(1e-7, 0.4)	0.05923	(0.05696, 0.06139)	-1.57
p_7^*	$\mathcal{U}$(-7, 3)	0.0002949	(0.0002315, 0.000421)	-1.665
p_8	$\mathcal{U}$(1e-7, 0.4)	0.08746	(0.08027, 0.08944)	-1.478

Supplementary Table 17: Summary of results for parameters of standardised I_{to} model using unified dataset. *Parameters were searched in $\log_{10}$ space and are presented in linear space. The prior for these parameters is still in the original $\log_{10}$ space.

S4.4 I_{Kur}

$$
\begin{aligned}
I_{\mathrm{sus}} &= \bar{g}_{\mathrm{sus}} r_{\mathrm{sus}} s_{\mathrm{sus}} \left(\mathrm{V} - \mathrm{E_K}\right) \\
\frac{\mathrm{d}r_{\mathrm{sus}}}{\mathrm{dt}} &= \frac{\overline{r_{\mathrm{sus}}} - r_{\mathrm{sus}}}{\tau_{r_{\mathrm{sus}}}}, \qquad \frac{\mathrm{d}s_{\mathrm{sus}}}{\mathrm{dt}} = \frac{\overline{s_{\mathrm{sus}}} - s_{\mathrm{sus}}}{\tau_{s_{\mathrm{sus}}}} \\
\overline{r_{\mathrm{sus}}} &= \frac{1.0}{1.0 + e^{(\mathrm{V}+\mathbf{p_1})/-\mathbf{p_2}}}, \qquad \tau_{r_{\mathrm{sus}}} = 1000 \left(\frac{\mathbf{p_3}}{1.0 + e^{(\mathrm{V}+\mathbf{p_4})/\mathbf{p_5}}} + \mathbf{p_6} \right) \\
\overline{s_{\mathrm{sus}}} &= \frac{1.0 - \mathbf{q_3}}{1.0 + e^{(\mathrm{V}+\mathbf{q_1})/\mathbf{q_2}}} + \mathbf{q_3}, \qquad \tau_{s_{\mathrm{sus}}} = 1000 \left(\frac{\mathbf{q_4}}{1.0 + e^{(\mathrm{V}+\mathbf{q_5})/\mathbf{q_6}}} + \mathbf{q_7} \right)
\end{aligned}
$$

Supplementary Table 18: Gating kinetics in Nygren model of I_{sus} (I_{Kur}) channel current (see Table 8 in [1]). Time constants are multiplied by 1000 to convert from s to ms.

		Original				Unified		
Name	Published	Prior	Median	89% HDPI	$\log_{10}$RSD	Median	89% HDPI	$\log_{10}$RSD
p1	4.3	$\mathcal{U}$(-100, 100)	1.895	(1.821, 1.946)	-1.68	2.031	(1.996, 2.056)	-2.028
p2	8.0	$\mathcal{U}$(1e-7, 50)	4.54	(4.487, 4.564)	-2.226	4.305	(4.295, 4.325)	-2.61
p3*	0.009	$\mathcal{U}$(-5, 0)	0.004119	(0.004024, 0.004169)	-2.667	0.002799	(0.002775, 0.002824)	-3.017
p4	5.0	$\mathcal{U}$(-100, 100)	-13.6	(-14.2, -13.1)	-1.582	-19.02	(-19.31, -18.77)	-2.056
p5	12.0	$\mathcal{U}$(1e-7, 50)	7.566	(7.169, 7.953)	-1.496	5.109	(4.959, 5.271)	-1.709
p6*	0.0005	$\mathcal{U}$(-6, -1)	0.0007858	(0.0007327, 0.0008531)	-2.147	0.0008455	(0.0008235, 0.0008719)	-2.58
q1	20.0	$\mathcal{U}$(-100, 100)	21.14	(8.065, 51.78)	-0.1842	21.14	(8.065, 51.78)	-0.1842
q2	10.0	$\mathcal{U}$(1e-7, 50)	12.96	(0.8947, 27.71)	-0.2282	12.96	(0.8947, 27.71)	-0.2282
q3	0.6	$\mathcal{U}$(0, 1)	0.121	(0.0001271, 0.268)	-0.1557	0.121	(0.0001271, 0.268)	-0.1557
q4*	0.047	$\mathcal{U}$(-4, 1)	0.06416	(0.01542, 0.133)	-0.6109	0.06416	(0.01542, 0.133)	-0.6109
q5	60.0	$\mathcal{U}$(-100, 100)	43.27	(-52.21, 99.65)	0.2045	43.27	(-52.21, 99.65)	0.2045
q6	10.0	$\mathcal{U}$(1e-7, 50)	27.02	(1.936, 45.79)	-0.238	27.02	(1.936, 45.79)	-0.238
q7*	0.3	$\mathcal{U}$(-3, 2)	0.286	(0.2161, 0.3196)	-0.221	0.286	(0.2161, 0.3196)	-0.221

Supplementary Table 19: Summary of results for parameters of Nygren I_{Kur} model. Only activation parameters (p) were recalibrated to unified dataset. *Parameters were searched in $\log_{10}$ space based on the scale of their published values and are presented in linear space. The prior for these parameters is still in the original $\log_{10}$ space.

$$I_{\mathrm{Kur}} = g_{\mathrm{Kur}} \left(1.0 + \frac{\mathbf{r_1}}{1.0 + e^{(V+\mathbf{r_2})/-\mathbf{r_3}}}\right) u_{\mathrm{a}}^3 u_{\mathrm{i}} \left(\mathrm{V} - \mathrm{E_K}\right)$$

$$\frac{\mathrm{d}u_{\mathrm{a}}}{\mathrm{dt}} = \frac{u_{\mathrm{a}(\infty)} - u_{\mathrm{a}}}{\tau_{u(\mathrm{a})}}, \qquad \frac{\mathrm{d}u_{\mathrm{i}}}{\mathrm{dt}} = \frac{u_{\mathrm{i}(\infty)} - u_{\mathrm{i}}}{\tau_{u(\mathrm{i})}}$$

$$u_{\mathrm{a}(\infty)} = \frac{1.0}{1.0 + e^{(\mathrm{V}+\mathbf{p_1})/-\mathbf{p_2}}}, \qquad \alpha_{u(\mathrm{a})} = \frac{\mathbf{p_3}}{e^{(\mathrm{V}+\mathbf{p_4})/-\mathbf{p_5}} + e^{(\mathrm{V}+\mathbf{p_6})/-\mathbf{p_7}}}, \qquad \beta_{u(\mathrm{a})} = \frac{\mathbf{p_3}}{\mathbf{p_8} + e^{(\mathrm{V}+\mathbf{p_9})/\mathbf{p_{10}}}}$$

$$u_{\mathrm{i}(\infty)} = \frac{1.0}{1.0 + e^{(\mathrm{V}+\mathbf{q_1})/\mathbf{q_2}}}, \qquad \alpha_{u(\mathrm{i})} = \frac{1.0}{\mathbf{q_3} + e^{(\mathrm{V}+\mathbf{q_4})/-\mathbf{q_5}}}, \qquad \beta_{u(\mathrm{i})} = e^{(\mathrm{V}+\mathbf{q_6})/\mathbf{q_7}}$$

$$\tau_\phi = \left(\alpha_\phi + \beta_\phi\right)^{-1}, \qquad \text{for } \phi = u_{\mathrm{a}}, u_{\mathrm{i}}$$

Supplementary Table 20: Gating kinetics in Courtemanche model of I_{Kur} channel current (see Appendix in [2]).

			Original			Unified		
Name	Published	Prior	Median	89% HDPI	$\log_{10}$RSD	Median	89% HDPI	$\log_{10}$RSD
p1	30.3	$\mathcal{U}$(-100, 100)	22.15	(20.09, 24.22)	-1.213	22.15	(20.09, 24.22)	-1.213
p2	9.6	$\mathcal{U}$(1e-7, 50)	17.41	(13.63, 21.67)	-0.8446	17.41	(13.63, 21.67)	-0.8446
p3*	0.65	$\mathcal{U}$(-3, 2)	0.04404	(0.00102, 0.1094)	-0.4886	0.04404	(0.00102, 0.1094)	-0.4886
p4	10.0	$\mathcal{U}$(-100, 100)	32.29	(-4.553, 88.19)	-0.1005	32.29	(-4.553, 88.19)	-0.1005
p5	8.5	$\mathcal{U}$(1e-7, 50)	16.13	(3.228, 37.54)	-0.2495	16.13	(3.228, 37.54)	-0.2495
p6	-30.0	$\mathcal{U}$(-100, 100)	32.82	(-2.739, 87.54)	-0.1255	32.82	(-2.739, 87.54)	-0.1255
p7	59.0	$\mathcal{U}$(1e-7, 50)	16.26	(1.388, 32.48)	-0.2607	16.26	(1.388, 32.48)	-0.2607
p8*	2.5	$\mathcal{U}$(-3, 2)	0.06393	(0.001001, 0.5319)	-0.1877	0.06393	(0.001001, 0.5319)	-0.1877
p9	82.0	$\mathcal{U}$(-100, 100)	47.77	(-22.92, 99.54)	0.04513	47.77	(-22.92, 99.54)	0.04513
p10	17.0	$\mathcal{U}$(1e-7, 50)	41.82	(29.25, 49.78)	-0.6841	41.82	(29.25, 49.78)	-0.6841
r1*	10.0	$\mathcal{U}$(0, 2)	8.721	(1.004, 61.18)	-0.2278	8.721	(1.004, 61.18)	-0.2278
r2	-15.0	$\mathcal{U}$(-100, 100)	-6.353	(-84.56, 87.51)	1.22	-6.353	(-84.56, 87.51)	1.22
r3	13.0	$\mathcal{U}$(1e-7, 50)	25.3	(0.04052, 44.01)	-0.231	25.3	(0.04052, 44.01)	-0.231
q1	-99.45	$\mathcal{U}$(-200, 200)	-69.32	(-144.5, -0.2399)	-0.1766	54.84	(54.83, 54.85)	-3.809
q2	27.48	$\mathcal{U}$(1e-7, 50)	34.61	(15.72, 49.44)	-0.4477	39.95	(39.94, 39.96)	-3.968
q3*	21.0	$\mathcal{U}$(-1, 4)	1941.0	(0.1185, 5866.0)	-0.319	674.0	(674.0, 674.0)	-5.458
q4	-185.0	$\mathcal{U}$(-200, 200)	-118.8	(-199.4, -34.61)	-0.2815	74.15	(72.39, 81.09)	-1.373
q5	28.0	$\mathcal{U}$(1e-7, 50)	26.47	(0.6525, 43.54)	-0.2649	3.708	(2.084, 4.118)	-0.6464
q6	-158.0	$\mathcal{U}$(-200, 0)	-172.1	(-199.5, -133.3)	-0.8272	-151.0	(-199.9, -95.79)	-0.6078
q7	16.0	$\mathcal{U}$(1e-7, 50)	23.66	(14.8, 28.97)	-0.5748	1.984	(0.03531, 4.561)	-0.1569

Supplementary Table 21: Summary of results for parameters of Courtemanche I_{Kur}. Only inactivation parameters (q) were recalibrated to unified dataset. *Parameters were searched in $\log_{10}$ space based on the scale of their published values and are presented in linear space. The prior for these parameters is still in the original $\log_{10}$ space.

Unified				
Name	Prior	Median	89% HDPI	$\log_{10}$RSD
p_1^*	$\mathcal{U}$(-7, 3)	0.0558	(0.0433, 0.06443)	-1.367
p_2	$\mathcal{U}$(1e-7, 0.4)	0.1464	(0.1281, 0.1683)	-1.043
p_3^*	$\mathcal{U}$(-7, 3)	0.1188	(0.1096, 0.1279)	-1.634
p_4	$\mathcal{U}$(1e-7, 0.4)	0.02021	(0.01904, 0.02213)	-1.306
p_5^*	$\mathcal{U}$(-7, 3)	0.004436	(0.004311, 0.004566)	-2.485
p_6	$\mathcal{U}$(1e-7, 0.4)	0.001568	(0.001221, 0.001863)	-0.8671
p_7^*	$\mathcal{U}$(-7, 3)	1.424e-07	(1.005e-07, 3.607e-07)	-1.417
p_8	$\mathcal{U}$(1e-7, 0.4)	0.02784	(0.02351, 0.03098)	-1.079

Supplementary Table 22: Summary of results for parameters of standardised I_{Kur} model using unified dataset. *Parameters were searched in $\log_{10}$ space and are presented in linear space. The prior for these parameters is still in the original $\log_{10}$ space.

References

[1] A. Nygren, C. Fiset, L. Firek, J. W. Clark, D. S. Lindblad, R. B. Clark, and W. R. Giles, "Mathematical model of an adult human atrial cell: the role of K+ currents in repolarization," *Circulation Research*, vol. 82, pp. 63–81, Jan. 1998.

[2] M. Courtemanche, R. J. Ramirez, and S. Nattel, "Ionic mechanisms underlying human atrial action potential properties: insights from a mathematical model," *The American Journal of Physiology*, vol. 275, no. 1, pp. H301–321, 1998.

[3] Y. Sakakibara, J. A. Wasserstrom, T. Furukawa, H. Jia, C. E. Arentzen, R. S. Hartz, and D. H. Singer, "Characterization of the sodium current in single human atrial myocytes," *Circulation Research*, vol. 71, pp. 535–546, Sept. 1992.

[4] M. Schneider, T. Proebstle, V. Hombach, A. Hannekum, and R. Rdel, "Characterization of the sodium currents in isolated human cardiocytes," *Pflugers Archiv: European Journal of Physiology*, vol. 428, pp. 84–90, Aug. 1994.

[5] T. Mewes and U. Ravens, "L-type Calcium Currents of Human Myocytes from Ventricle of Non-failing and Failing Hearts and from Atrium," *Journal of Molecular and Cellular Cardiology*, vol. 26, pp. 1307–1320, Oct. 1994.

[6] G. R. Li and S. Nattel, "Properties of human atrial ICa at physiological temperatures and relevance to action potential," *The American Journal of Physiology*, vol. 272, pp. H227–235, Jan. 1997.

[7] H. Sun, N. Leblanc, and S. Nattel, "Mechanisms of inactivation of L-type calcium channels in human atrial myocytes," *The American Journal of Physiology*, vol. 272, pp. H1625–1635, Apr. 1997.

[8] E. F. Shibata, T. Drury, H. Refsum, V. Aldrete, and W. Giles, "Contributions of a transient outward current to repolarization in human atrium," *American Journal of Physiology-Heart and Circulatory Physiology*, vol. 257, pp. H1773–H1781, Dec. 1989.

[9] Z. Wang, B. Fermini, and S. Nattel, "Sustained depolarization-induced outward current in human atrial myocytes. Evidence for a novel delayed rectifier K+ current similar to Kv1.5 cloned channel currents," *Circulation Research*, vol. 73, pp. 1061–1076, Dec. 1993.

[10] L. Firek and W. R. Giles, "Outward currents underlying repolarization in human atrial myocytes," *Cardiovascular Research*, vol. 30, pp. 31–38, July 1995.

[11] K. H. W. J. ten Tusscher, D. Noble, P. J. Noble, and A. V. Panfilov, "A model for human ventricular tissue," *American Journal of Physiology. Heart and Circulatory Physiology*, vol. 286, pp. H1573–1589, Apr. 2004.

[12] T. Toni, D. Welch, N. Strelkowa, A. Ipsen, and M. P. H. Stumpf, "Approximate Bayesian computation scheme for parameter inference and model selection in dynamical systems," *Journal of the Royal Society, Interface*, vol. 6, pp. 187–202, Feb. 2009.

[13] G. R. Mirams, P. Pathmanathan, R. A. Gray, P. Challenor, and R. H. Clayton, "Uncertainty and variability in computational and mathematical models of cardiac physiology," *The Journal of Physiology*, vol. 594, no. 23, pp. 6833–6847, 2016.

[14] K. A. Beattie, A. P. Hill, R. Bardenet, Y. Cui, J. I. Vandenberg, D. J. Gavaghan, T. P. de Boer, and G. R. Mirams, "Sinusoidal voltage protocols for rapid characterisation of ion channel kinetics," *The Journal of Physiology*, vol. 596, no. 10, pp. 1813–1828, 2018.